



UNIVERSIDADE FEDERAL DE SANTA CATARINA  
CENTRO TECNOLÓGICO, DE CIÊNCIAS EXATAS E EDUCAÇÃO  
COORDENADORIA ESPECIAL DE ENGENHARIA DE MATERIAIS  
CURSO DE ENGENHARIA DE MATERIAIS

Ádria Cypriano

**Design and development of an aluminum brazing process with Penetration Depth  
Induction**

Blumenau

2024

Ádria Cypriano

**Design and development of an aluminum brazing process with Penetration Depth  
Induction**

Final paper submitted in partial fulfillment of the requirements for the degree of BEng. In Materials Engineering of the Universidade Federal de Santa Catarina.

Advisor: Prof. Dr. Wanderson Santana da Silva  
Co-advisor: Eng. Thomas Vauderwange

Blumenau

2024

Cypriano, Ádria

Design and development of an aluminum brazing process with Penetration Depth Induction / Ádria Cypriano ; orientador, Wanderson Santana da Silva, coorientador, Thomas Vauderwange, 2024.

85 p.

Trabalho de Conclusão de Curso (graduação) - Universidade Federal de Santa Catarina, Campus Blumenau, Graduação em Engenharia de Materiais, Blumenau, 2024.

Inclui referências.

1. Engenharia de Materiais. 2. Brasagem. 3. Indução. 4. Alumínio. I. Silva, Wanderson Santana da. II. Vauderwange, Thomas. III. Universidade Federal de Santa Catarina. Graduação em Engenharia de Materiais. IV. Título.

Ádria Cypriano

**Design and development of an aluminum brazing process with Penetration Depth Induction**

Final paper submitted in partial fulfillment of the requirements for the degree of BEng. in Materials Engineering of the Universidade Federal de Santa Catarina.

Blumenau, 2 de Dezembro de 2024.

Insira neste espaço  
a assinatura

Ádria Cypriano  
Acadêmica

**Banca examinadora**

Insira neste espaço  
a assinatura

Prof. Dr. Wanderson Santana da Silva  
Orientador

Insira neste espaço  
a assinatura

Prof. Dra. Renata Braga Soares  
Instituição Universidade Federal de Santa Catarina

Insira neste espaço  
a assinatura

Prof. Msc. Daniel Fonseca da Cunha  
Instituição Universidade Federal de Santa Catarina

Blumenau, 2024.

I dedicate this work to my family, for always believing in my potential and for being constant sources of inspiration and motivation.

## ACKNOWLEDGEMENTS

I first thank God for the strength, health, and patience He granted me throughout my entire academic journey. Without His guidance, I would not have had the courage to face the challenges and embrace the opportunities that came my way.

To my parents, who are my foundation. Everything I am today and everything I have achieved is a reflection of the support, love, and values you gave me. You have always been my greatest inspiration. I owe everything to you — your sacrifices, your dreams for me, and your endless belief in my potential. This accomplishment is as much yours as it is mine.

To my brother, who has always been my role model both as a person and as a professional. From childhood to now, you've always been there, guiding me, teaching me, and being an example of strength and perseverance. You taught me not just how to play, but how to face life with courage and determination. You've had a significant impact on my journey, and for that, I will forever be grateful.

To Rodrigo, my safe harbor, who has always believed in me more than I believed in myself. Your confidence was one of the greatest drives to get me here. I cannot express how much your support has meant to me.

To my advisor, for his always helpful guidance, his genuine interest in my work, and for all the lessons taught. Your mentorship has made all the difference.

To my dear friend Adriana, my partner in college, profession, and life. From the very first day (first day indeed since we met in the entrance exam), you have been by my side, not only as a friend but as a sister. We've shared laughter, tears, and countless memories. Your friendship has been one of the most important gifts in my life.

To my long-time friend, teacher, and tango partner, Mario Brasil, who has always supported and encouraged me to pursue my dreams, offering advice and guidance at important moments.

To the friends who have walked this path with me, bringing joy and comfort during moments of uncertainty, especially my colleagues and the technicians from UFSC — Pablo, Derick, Daniel — who supported me throughout this work. A special thanks to Maiara and Antonio from WEG Equipamentos Elétricos for their valuable assistance with the SEM tests.

To the Vauquadrat team, especially Mr. Vauderwange, for the opportunity and trust, and to Benjamin Kloos, for always being willing to help whenever I needed it. This experience made a significant difference during my exchange program, and I truly appreciate the chance to learn with you.

Finally, to the professors and everyone who, in some way, contributed to my academic and personal growth. Each one of you is part of this achievement.

*“I’ve done my best, and I begin to understand what is meant by ‘the joy of strife’. Next to trying and winning, the best thing is trying and failing.”*  
— L.M. Montgomery



## RESUMO

Técnicas de união de materiais, como a soldagem, são essenciais em setores como o automotivo e aeroespacial. No entanto, quando se trata de alumínio, a soldagem enfrenta desafios devido à formação de óxidos e características térmicas do material. Nesse contexto, o método de brasagem, especialmente por indução, destaca-se, pois permite a união de componentes de alumínio sem fundi-los, por meio da adição de uma liga de brasagem, que funde e forma a junta. Este trabalho tem como objetivo desenvolver um processo de brasagem por indução por penetração profunda de tubos de alumínio da liga 3103 utilizados em trocadores de calor de sistemas de refrigeração, com foco nos parâmetros de processo (frequência, tempo, potência e modulação da largura de pulso). Inicialmente, projetou-se um indutor de cobre adequado à geometria dos tubos, buscando aquecimento uniforme e eficiente. Foram realizados testes com a liga de adição Filalu 1192, composta pela liga 4047A e fluxo de fluorossilicato de potássio, variando a potência e o tempo para duas abordagens de brasagem por indução: uma com potência constante e outra em duas etapas, reduzindo a potência após um pico inicial para evitar superaquecimento. Testes em tubos com diferentes espessuras permitiram identificar os parâmetros ideais de brasagem, incluindo uma abordagem de duas etapas, que foi o melhor parâmetro encontrado: alta potência inicial (100% por 10 s), seguida de redução para 65% pelo restante do tempo, utilizando um capacitor de 6  $\mu\text{F}$ , frequência de 15,8 kHz e pulso de 8  $\mu\text{s}$ . Esse parâmetro proporcionou um bom preenchimento da junta e um tempo de brasagem adequado. Para comparar os métodos, também foi realizada a brasagem por chama. Avaliações da qualidade das juntas incluíram inspeção visual, microscopia óptica e eletrônica (MEV), análise química (EDS) e ensaios de tração. A inspeção visual permitiu ajustar os parâmetros ao identificar defeitos como excesso ou falta de material, superaquecimento e desalinhamento. As análises microscópicas mostraram uma distribuição adequada do material de enchimento na maioria das amostras, com exceções que apresentaram preenchimento incompleto. Imagens da interface das juntas por MEV revelaram porosidade e microestruturas dendríticas, enquanto o EDS confirmou a composição e a distribuição de alumínio e silício na área de fusão. Os resultados dos ensaios de tração indicaram variações significativas na resistência à tração e deformação entre os grupos amostrais. A amostra sem brasagem apresentou a maior resistência à tração, atingindo 53,16 MPa, enquanto as amostras brasadas exibiram resistência inferior, chegando a 37,81 MPa, um valor consistente com outras referências, embora inferior ao do tubo sem brasagem. As curvas tensão-deformação evidenciaram que as amostras brasadas suportam forças significativas sem fraturar na junta, sugerindo que a resistência à tração da junta era superior à do próprio tubo. A pressão máxima suportável pelos tubos foi calculada usando a equação de Lamé, com um resultado mínimo de 26,8 bar.

**Palavras-chave:** ligas de alumínio; indução; brasagem; trocadores de calor.

## ABSTRACT

Material joining techniques, like welding, are essential in fields such as automotive and aerospace. However, when it comes to aluminum, welding faces challenges due to oxide formation and the material's thermal properties. In this context, brazing, especially induction brazing, stands out, as it allows aluminum components to be joined without melting them. This is done by adding a brazing alloy that melts to form the joint. This study aims to develop a depth penetration induction brazing process for aluminum 3103 tubes used in heat exchangers for cooling systems, focusing on process parameters like frequency, time, power, and pulse width modulation. To start, a copper inductor was designed to match the geometry of the tubes, aiming for homogeneous and efficient heating. Tests were carried out with Filalu 1192 filler alloy, made of 4047A alloy with potassium fluoroaluminate flux, adjusting power and time for two induction brazing methods: one with constant power and another in two stages, reducing power after an initial peak to avoid overheating. Tests on tubes with different wall thicknesses allowed for the identification of the ideal brazing parameters, including a two-step approach, which was the best parameter found: high initial power (100% for 10 s), followed by a reduction to 65% for the rest of the process, using a 6  $\mu\text{F}$  capacitor, 15.8 kHz frequency, and an 8  $\mu\text{s}$  pulse. This parameter provided good joint filling and an adequate brazing time. Joint quality was examined through visual inspection, optical and electron microscopy (SEM), chemical analysis (EDS), and tensile testing. Visual inspection helped refine the parameters by identifying defects such as excess or lack of material, overheating, and misalignment. Microscopic analysis showed good filler distribution in most samples, except for a few with incomplete filling. SEM images of joint interfaces revealed porosity and dendritic microstructures, while EDS confirmed the aluminum and silicon composition in the fusion area. Tensile tests showed notable differences in strength and strain among sample groups. The unbrazed sample had the highest strength, reaching 53.16 MPa, while brazed samples showed lower strength, reaching 37.81 MPa—a consistent value with other references, though lower than the unbrazed tube. The stress-strain curves indicated that brazed samples withstood significant forces without joint fracture, suggesting that the joint strength was higher than that of the tube itself. The tube's maximum withstandable pressure was calculated using Lamé's equation with a minimum result of 26,8 bar.

**Keywords:** aluminum alloys; induction; brazing; heat exchangers.

## LIST OF FIGURES

Figure 1 – Surface energies of a liquid droplet	20
Figure 2 – Capillary force between two walls	22
Figure 3 – Principle of inductive heating	26
Figure 4 – Current density distribution and heating	27
Figure 5 – Electrical resistivity of commercial metals	28
Figure 6 – Exploded view of an inductor	30
Figure 7 – Magnetic field a) without and b) with field concentrators	31
Figure 8 – Dendrites in Al-20% Cu Liquid	34
Figure 9 – Dendrites arms, primary $\lambda_1$ , secondary $\lambda_2$ and tertiary $\lambda_3$ arm spacings	35
Figure 10 – Phase diagram of Al and Mn	36
Figure 11 – 3003 alloy a) polished and b) etched	37
Figure 12 – Phase diagram of Al and Si	38
Figure 13 – Filling of the joint with a) ring without intern flux, b) ring with intern flux and c) brazing paste	40
Figure 14 – Microstructure of brazed region with a) ring without intern flux and b) brazing paste	40
Figure 15 – a) Tubes, b) rings and c) field enhancers used	42
Figure 16 – Schematic drawing of the induction brazing system	43
Figure 17 – Software Output Over Time	44
Figure 18 – a) Manually fabricated inductor and b) burned tube	45
Figure 19 – Technical drawing of the printed part of inductor - 4GYD32	46
Figure 20 – a) TIG welding and b) finished inductor	46
Figure 21 – a) One side is not brazed while the other is and b) one side brazed while the other burns	47
Figure 22 – Technical drawing of the printed part of inductor - 4GYD33	47
Figure 23 – Technical drawing of the printed part of inductor - 4GYD36	48
Figure 24 – Finished 2.NY 287 inductor	49
Figure 25 – a) Metal sheet and b) ceramic blocks	49
Figure 26 – Sample prepared for microscopic analysis	52
Figure 27 – Tensile test samples	54
Figure 28 – Samples from a) group A and b) group B	56
Figure 29 – Microstructural analysis of sample A1 a) 50x of the overall joint; b) 50x of the upper side of the joint; c) 200x of the middle section; d) 200x of the lower part	56
Figure 30 – Microstructural analysis of Sample A2 a) 50x of the overall joint; b) 50x of the lower side of the joint; c) 200x of the lower part; d) 200x of dendrite	57
Figure 31 – Microstructural analysis of Sample B1 a) 50x of the lower side of the joint; b) 50x of the upper part; c) 100x of the lower part; d) 200x of the middle part	58
Figure 32 – Microstructural analysis of Sample C1 a) 50x of the upper side of the joint; b) 50x of the overall joint; c) 200x of the void; d) 500x	59
Figure 33 – Microscopy of the filler metal	62

Figure 34 – SEM images of sample A2 a) 150x and b) 500x	62
Figure 35 – EDS of sample A2	63
Figure 36 – SEM images of sample F2 a) 150x; b) 500x ; c) void; d) incomplete filling	64
Figure 37 – EDS of sample F2	65
Figure 38 – SEM images of sample C1 a) overall; b) void	65
Figure 39 – EDS of sample C1	66
Figure 40 - Graph of 95% confidence intervals for average tensile strength	68
Figure 41 - Graph of 95% confidence intervals for average deformation	69
Figure 42 – Stress Strain Curves for Group I	70
Figure 43 – Observed failure in Group I a) sample A; b) sample F	70
Figure 44 – Stress Strain Curves for Group II	71
Figure 45 – Stress Strain Curves for Group III	72
Figure 46 – Stress Strain Curves for Group IV	72
Figure 47 – Stress Strain Curves for Group V	73
Figure 48 – Fracture surfaces of aluminum tubes a) without and b) with brazing	74

## **LIST OF BOXES**

Box 1 – Summary of Filling Characteristics and Defect Presence for Each Sample

59

## LIST OF TABLES

Table 1 – Brazing parameters	29
Table 2 – Main alloying elements in the wrought alloy designation system	33
Table 3 – Chemical composition of 3103 alloy	41
Table 4 – Average dimensions of the tube	41
Table 5 – Chemical composition of 4047Aalloy	42
Table 6 – Power settings and brazing time	51
Table 7 – Sample parameters	52
Table 8 – Sample parameters for tensile test	54
Table 9 – Average mechanical properties	67
Table 10 – Maximum Allowable Pressure Based on Tensile Strength	75

## **LIST OF ABBREVIATIONS AND ACRONYMS**

ANSI	American National Standards Institute
EDS	Energy Dispersive X-ray Spectroscopy
ISO	International Organization for Standardization
LAMEA	Microscopy and Structural Analysis Laboratory
SEM	Scanning Electron Microscopy
UST	Ultimate Tensile Strength
WD	Working Distance

## LIST OF SYMBOLS

$\gamma_{SL}$	surface tension of a liquid
$\gamma_{SV}$	surface tension of a solid
$\gamma_{LV}$	interfacial tension between solid and liquid
$\theta$	angle of contact
$W_a$	work of adhesion
$h$	height of rising liquid
$\rho$	density
$g$	gravity
$\Phi$	magnetic flux
$I_k$	eddy current
$\delta$	current penetration depth
$\mu_r$	relative permeability
$f$	frequency
Al- $\alpha$	alpha aluminum
$\sigma_{UTS}$	ultimate tensile strength
$\varepsilon$	total strain



## TABLE OF CONTENTS

<b>1 INTRODUCTION</b>	<b>16</b>
1.1 OBJECTIVES	17
<b>1.1.1 Main Objective</b>	<b>17</b>
<b>1.1.2 Specific Objectives</b>	<b>17</b>
<b>2 THEORETICAL BACKGROUND</b>	<b>18</b>
2.1 BRAZING	18
<b>2.1.1 Overview</b>	<b>18</b>
<b>2.1.2 Fundamentals</b>	<b>19</b>
2.1.2.1 Wetting	19
2.1.2.2 Capillarity	21
<b>2.1.3 Base materials</b>	<b>22</b>
<b>2.1.4 Brazing alloys</b>	<b>23</b>
<b>2.1.5 Flux</b>	<b>24</b>
<b>2.1.6 Flame brazing</b>	<b>25</b>
<b>2.1.7 Induction brazing</b>	<b>25</b>
2.1.7.1 <i>Induction heating</i>	25
2.1.7.2 <i>Process parameters</i>	29
<b>2.1.8 Brazing defects</b>	<b>31</b>
2.2 ALUMINUM ALLOYS	32
<b>2.2.1 Aluminum Solidification</b>	<b>33</b>
<b>2.2.2 3XXX series</b>	<b>35</b>
<b>2.2.3 4XXX series</b>	<b>37</b>
<b>2.2.4 Aluminum Brazing</b>	<b>39</b>
<b>3 MATERIALS AND METHODS</b>	<b>41</b>
3.1 MATERIALS	41
3.2 METHODS	42
<b>3.2.1 Flame brazing</b>	<b>42</b>
<b>3.2.2 Induction brazing</b>	<b>43</b>
<b>3.2.3 Development of inductors</b>	<b>45</b>
3.3 CHARACTERIZATION	51
<b>3.3.1 Samples preparation</b>	<b>51</b>
<b>3.3.2 Visual inspection</b>	<b>53</b>
<b>3.3.3 Optical Microscopy</b>	<b>53</b>
<b>3.3.4 Scanning Electron Microscopy and Energy Dispersive Spectroscopy</b>	<b>53</b>
<b>3.3.5 Tensile test</b>	<b>53</b>
<b>3.3.6. ANOVA</b>	<b>54</b>
<b>4 RESULTS AND DISCUSSION</b>	<b>55</b>
4.1 VISUAL INSPECTION	55
4.2 MICROSCOPY	56

4.3 SEM – EDS	62
4.4 TENSILE TEST	66
<b>5 CONCLUSION</b>	<b>75</b>
<b>6 RECOMMENDATIONS FOR FUTURE WORK</b>	<b>77</b>
<b>REFERÊNCIAS</b>	<b>78</b>

## 1 INTRODUCTION

Aluminum alloys are used in many applications in the automotive, aerospace, and other industries because of their combination of corrosion resistance, lightweight, specific strength and thermal conductivity (Hosch & Napolitano, 2010; Çam & İpekoğlu, 2016). These properties make aluminum alloys interesting for the fabrication of heat exchangers in refrigeration systems, between those alloys, the 3XXX, designation from ANSI (2017), series are the most common for this application. This series of alloys contains manganese, which increases mechanical strength and hardness (Hosch and Napolitano, 2010).

In industrial applications joining techniques are important for assembling components, and the methods used include welding, mechanical fastening, soldering and brazing, the last two differing on the temperature applied. However, when it comes to aluminum, especially in heat exchanger tubes, brazing is a preferred technique. The formation of an oxide layer, aluminum's thermal conductivity and melting characteristics are challenges when welding aluminum (Çam and İpekoğlu, 2016). That is why brazing offers the advantage of creating joints that do not leak while maintaining the integrity of the base material. Among brazing methods, induction brazing is effective due to its precision, speed, and ability to control heat input, which is essential when working with temperature-sensitive materials like aluminum (Zhao *et al.*, 2021).

Brazing is a joining process that creates a bond by introducing and melting a filler metal between the components. The filler metal must have a melting temperature above 450°C and below the melting point of the base materials. Therefore, only the filler melts, and not the base material. This technique allows joining different materials with minimal interference in the base material, reducing thermal distortions (Way, Willingham and Goodall, 2019).

Induction brazing is a complex process that uses the principles of electromagnetism. Many parameters can affect the quality and the viability of the process, such as power, shape of inductor, joint gap, materials properties and others. For aluminum, induction brazing is a major challenge due to the small difference between the melting points of the filler and the base metal (Çam; İpekoğlu, 2016; Rudnev; Loveless and Cook, 2017). The motivation for this work comes from the opportunity to enhance the quality and productivity of joining techniques for aluminum heat exchanger tubes. The difficulties faced in welding aluminum further amplify the importance of induction brazing. Therefore, the goal is to evaluate the

effectiveness of induction brazing on aluminum tubes, focusing on optimizing process parameters and ensuring consistent filler metal coverage to improve joint performance.

## 1.1 OBJECTIVES

### 1.1.1 Main Objective

Design and develop an induction brazing process for aluminum tubes with penetration depth, aiming the applications in the manufacturing of heat exchangers for refrigeration systems.

### 1.1.2 Specific Objectives

- Develop an appropriate copper inductor.
- Evaluate the effect of induction brazing parameters (time and power) on the joint, using optical microscopy.
- Assess the coverage of the filler metal and the presence of defects.
- Perform microstructural characterization of the brazed region, using optical and electronic microscopy.
- Evaluate mechanical properties using tensile tests.

## 2 THEORETICAL BACKGROUND

### 2.1 BRAZING

#### 2.1.1 Overview

In many everyday applications, joining two or more components is essential, and techniques such as welding, brazing and soldering are used for that. To select the appropriate joining method, some factors and requirements must be taken into consideration, such as operating temperature, materials to be joined, corrosion resistance, mechanical properties, costs, etc (Schwartz, 2003; Kakitani, 2021).

Brazing is a type of joining technique based on the heating of materials in the presence of a filler metal at a temperature above 450°C and below the melting temperature of the base material. In this process, when the filler melts, it distributes and covers the area between the materials, by capillary action, creating a bond (Schwartz, 2003).

Both brazing and soldering use a filler metal, but they differ on the temperatures applied. Different from brazing, soldering happens at working temperatures below 450°C. In both cases, only the filler metal melts, unlike welding, where there is no filler and the base metal is the one that melts (Schwartz, 2003; Kakitani, 2021).

Brazing technology dates back to over 6000 years (Peter, 2014). As Schwartz (2003) says, brazing was developed by the need to join two metal pieces to produce structures that were not possible with the methods that existed, and metalworkers observed they could use a filler between the pieces of the base metal for that.

By that time, materials such as lead, tin, silver, and copper-arsenic were used as fillers due to their low melting points and were the only options available for years. After that, alloy brass started being used, providing joints with increased strength and temperature resistance. Also, the combination of brass and silver, when melted together, resulted in a lower melting point than brass alone, providing good adherence and better corrosion resistance (Schwartz, 2003).

Today, many alloys can be used as fillers, and their fluidity and wetting properties are important factors for their selection (Schwartz, 2003). Fluxes are added with the fillers to eliminate oxides and are a mixture of compounds that melts during the brazing process, forming a layer over the joint that reacts and removes the oxides. However, their main

purpose is to increase the wettability of the filler during the process (Way; Willingham and Goodall, 2019).

Brazing has many advantages, like less distortion compared to welding, excellent stress distribution, and the ability to join different materials, with different thicknesses (Schwartz, 2003; Kakitani, 2021). But it has limitations, like the formation of heterogeneous joints with different phases, resulting in diverse microstructures and properties, with unpredictable mechanical behavior (Schwartz, 2003). Besides that, joining complex components with sharp corners or threads is difficult, manual brazing is skill-dependent, and in the case of induction brazing, it requires a higher equipment cost (Way; Willingham and Goodall, 2019).

Brazing methods can be categorized by the heating source, including flame brazing, induction brazing, resistance brazing, and furnace brazing. There are special types of brazing such as infrared brazing, laser brazing, and plasma arc brazing (Li, Chen, Yi, and Ouyang, 2020). When compared to flame brazing, induction brazing offers some advantages such as the ability to heat without direct contact, fast and localized heating, high productivity, and the potential for automation (Way; Willingham and Goodall, 2019).

## **2.1.2 Fundamentals**

To understand brazing, it is necessary to study the fundamentals involved, such as wetting, adhesion, and capillary action.

### *2.1.2.1 Wetting*

During the brazing process, the filler material melts and wets the surface of the base material, and distributes itself into the space between the two components through capillary action. One important phenomenon responsible for brazing is wetting, which is the ability of a liquid to spread over a solid surface. A good wetting is important to ensure a strong and uniform joint between the pieces (Schwartz, 2003; Peter, 2014).

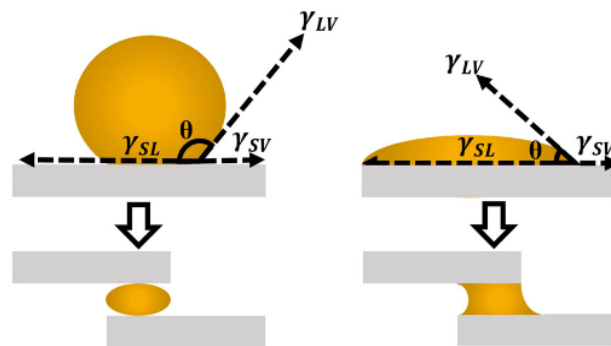
Thomas Young proposed an equation to describe the wetting of a liquid droplet on a solid surface, depending on three surface energies (Figure 1): the surface tension of a liquid ( $\gamma_{SL}$ ), in the case of brazing, the surface tension of the liquid solder; the surface free energy of

the solid base material ( $\gamma_{SV}$ ); and the interfacial tension between the solid surface (base material) and the liquid (solder) ( $\gamma_{LV}$ ) (Schwartz, 2003; Peter, 2014; Way; Willingham and Goodall, 2019). This relation is expressed by the Equation 1:

$$\gamma_{SV} = \gamma_{LV} \cos\theta + \gamma_{SL} \quad (1)$$

The angle  $\theta$  is the contact angle between the liquid and the solid, and it provides information about the quality of wetting. It should correspond to an angle lower than  $90^\circ$  for wetting and higher for non-wetting (Way; Willingham and Goodall, 2019). An angle of  $0^\circ$  corresponds to complete wetting, which is difficult to achieve in brazing because of surface roughness, cleanliness, the presence of oxides and impurities, temperature, and brazing time. Therefore, the wetting angle should be lower than  $20\text{-}30^\circ$  to generate good results (Peter, 2014; Way; Willingham and Goodall, 2019).

**Figure 1** – Surface energies of a liquid droplet



Source: Way, Willingham and Goodall, 2019.

The wetting is improved as the angle gets closer to  $0^\circ$ . Therefore, from Equation 1, it is evident that to reduce the angle,  $\gamma_{SV}$  must increase, or  $\gamma_{SL}$  and  $\gamma_{LV}$  decrease. The term  $\gamma_{SV}$  can be increased with clean surfaces. The presence of impurities, oils, lubricants, dust and oxides will reduce  $\gamma_{SV}$  and consequently increase  $\theta$ . To achieve cleanliness without oxides in the joint region, fluxes or protective atmospheres can be used (Jacobson and Humpston, 2005). In brazing, oxides are removed with the presence of fluxes, but their capacity is

limited, so the brazing process should not take too long to prevent the formation of too many oxides (Peter, 2014).

Research indicates that cleanliness and surface roughness affect the strength and reliability of the joint. Other studies point out that the smoother the surface, better the wetting and consequently the shear strength (Way, Willingham, and Goodall, 2019).

The term  $\gamma_{SL}$  is a constant between a solid-liquid combination, so it can be changed by altering composition of the alloys. This parameter depends on temperature and can be controlled by it.  $\gamma_{LV}$  is also constant for a given temperature and pressure, so it can be changed by modifying the composition of the atmosphere (Jacobson and Humpston, 2005).

The parameter of adhesion ( $W_a$ ) is also used to understand wetting. The Dupré equation, Equation 2, correlates de adhesion with the three surface energies:

$$W_a = \gamma_{LV} + \gamma_{SV} - \gamma_{SL} \quad (2)$$

So, the work of adhesion increases with increasing liquid-vapor and solid-vapor tension and decreases with decreasing solid-liquid tension. Equations 1 and 2 can be combined into the Young-Dupré equation, Equation 3, and then, the adhesion and angle of contact can be related (Jacobson and Humpston, 2005).

$$W_a = \gamma_{LV}(1 + \cos\theta) \quad (3)$$

#### 2.1.2.2 Capillarity

After the filler material melts, it goes into the space between the pieces, forming a cohesive bond without any voids or gaps, this process is facilitated by capillary action. This phenomenon is a result of the surface tension between the base metal, filler, flux, and the angle of wetting (Schwartz, 2003).

Capillary action refers to the tendency of a liquid to move along the walls of tubes or surfaces and makes possible that the liquid flows against gravity. It is also referred to as capillary filling pressure, which intensifies as the brazing gap or joint clearance gets narrower

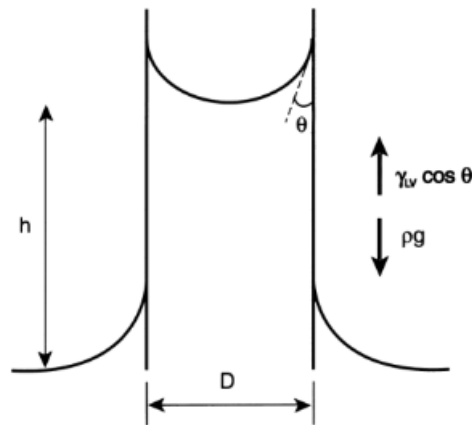


(Peter, 2014). The correlation between the height ( $h$ ) of rising liquid and the capillary filling pressure is given by the Equation 4 (Jacobson and Humpston, 2005):

$$h = \frac{2\gamma_{LV}\cos\theta}{g\cdot\rho\cdot D} \quad (4)$$

Where  $D$  is the joint clearance, as it can be seen in Figure 2,  $\rho$  is the filler density and  $g$  is the gravity. By this relation, the liquid will rise to a height where the capillary action equals the hydrostatic force (Jacobson and Humpston, 2005).

**Figure 2** – Capillary force between two walls



Source: Jacobson and Humpston, 2005.

Liang *et al.* (2022) indicate that brazing clearance should be less than 15 mm to achieve good capillary action and result in a brazed joint with good quality. Different sizes of joint clearance can result in varying microstructures and strengths. They also note that smaller clearances lead to higher tensile strength, while larger clearances increase the number and size of defects, as categorized by ISO 18279. So it is expected that the tightest joint clearance will result in the best filling and consequently the strongest brazed joint (Way, Willingham, and Goodall, 2019).

### 2.1.3 Base materials

In the brazing process, the materials being joined are called base materials, and their shape and structural properties should be maintained during the process. The most frequently used materials for that are metals and their alloys, such as steels, aluminum, and copper (Peter, 2014). The base material can be the same for the pieces being joined or consist of a mixed joint. The base material has an important effect on the strength of the brazed component, but there are complex reactions between the base metal and the filler, making the strength difficult to predict.

There are many alloy compositions for brazing, and their compositions are important for compatibility with the filler material and brazing-related phenomena. For instance, alloying can change the microstructure of the joint, improving or compromising its mechanical properties. Carbide precipitation can lead to localized hardness, which may result in stress concentrations and reduced joint strength. Stress cracking can occur due to residual stresses in the joint. Embrittlement caused by hydrogen, sulfur, and phosphorus can weaken the joint, making it more susceptible to failure under stress. Additionally, oxide stability is important in preventing the formation of oxides during the heating process, which can prevent proper wetting and bonding. Understanding these phenomena is essential for controlling the brazing process and ensuring the reliability of the joint (Schwartz, 2003).

#### **2.1.4 Brazing alloys**

The filler, or also known as brazing alloy, is responsible for bonding the base material and requires proper fluidity, stability, and wetting properties. The most common forms of filler include wire, wire rings, powder, and paste (Schwartz, 2003). There is a wide range of filler metals varying by their composition and melting ranges. The filler's melting range must be lower than that of the base material to prevent the base material from melting. The main types of fillers are aluminum-silicon, copper, silver, gold, nickel, palladium, and cobalt (Siqueira, 2021).

Several considerations must be taken into account for filler selection, including metallurgical compatibility between the filler and the base metal, operating temperature, mechanical loading, corrosion resistance requirements, wettability, brazing process and temperature, joint design, and toxicity (Way; Willingham and Goodall, 2019).

According to Peter (2014), for heavy metals, the fillers are typically non-ferrous alloys with copper, and sometimes silver. For high-temperature brazing, nickel-based alloys

are better, or even gold and palladium. Iron-based alloys, although less common, are used for steel, heat-resistant alloys, and cast iron. In aluminum brazing, aluminum-silicon fillers are more used because silicon can lower the melting point and improve wettability.

In aluminum brazing, the difference between the melting point of the filler and the base metal is low, requiring precise temperature control (Way; Willingham and Goodall, 2019). The most common alloys for brazing aluminum are from the 4xxx series, with a silicon content of around 7-14% and possessing good flow properties and a low thermal expansion coefficient (Kakitani, 2021).

The composition of the brazing alloy significantly impacts the brazing process. One key effect is related to wettability. An alloy that does not adequately wet the base material can result in discontinuities, such as incomplete filling or areas lacking adhesion, compromising the mechanical strength of the joint. Additionally, the alloy's composition affects its fluidity; alloys with poor fluidity can lead to porosity or internal voids, creating weak points that may fail under mechanical or thermal stress. Another common issue is the formation of brittle intermetallic compounds, particularly in alloys containing elements incompatible with the base material. For instance, in aluminum brazing, excessive copper or magnesium can lead to rigid intermetallic phases, making the joint more prone to fractures (Way; Willingham and Goodall, 2019).

### **2.1.5 Flux**

Besides the base metal and the filler, another important element for the brazing process is the flux. The flux is used to retard and remove the formation of oxides during heating and improve wetting and spreading of the filler. Flux consists of chemical compounds that when melted during the brazing process form a coating over the joint. This coating reacts with oxides, dissolving them and facilitating the bonding process. It can be a part of the filler or applied separately and is required in processes in air, since the metal is more susceptible to forming oxides when in contact with air. Flux can be in powder, paste, or liquid form (Siqueira, 2021; Way; Willingham and Goodall, 2019).

A good flux must melt at a temperature below the brazing temperature and be molten when the filler melts. It needs to flow through the joint to protect the surface and provide better wettability by reducing surface tension. Compounds found in fluxes typically include borates, boron, fluoborates, fluorides, chlorides, acids, and water (Vozniaki, 2014). Fluxes for

aluminum brazing are normally corrosive or require high temperatures. However, NOCOLOK® flux was developed with a mixture of potassium fluoroaluminates suitable for brazing temperatures and with the generation of non-corrosive residues (Milani, Tavangar, and Azadbeh, 2020). According to ISO 9454-1: 2016, NOCOLOK® is classified as an inorganic flux, based on fluorides and non-corrosive flux.

### **2.1.6 Flame brazing**

Flame brazing, also known as torch brazing, consists of heating the base material and filler with a flame generated by the combustion of oxygen and a gas, typically acetylene. This process can be done manually or automated with machines. It's a simple and low-cost method, often used in lower production volumes. A torch tip is necessary, as it's where the oxygen and gas mixture passes before creating the flame. Different combinations of gasses can be used depending on the required heat. Other frequently used gasses include oxyacetylene, oxyhydrogen, oxynatural, and others (Schwartz, 2003).

### **2.1.7 Induction brazing**

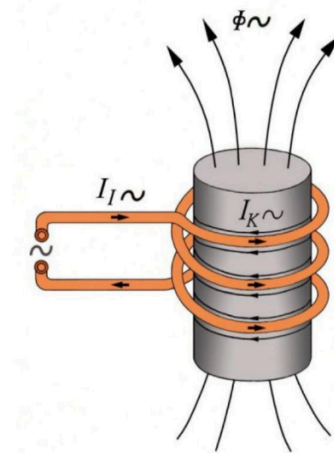
The principles of induction heating can be applied in many types of processes, such as heat treatment, mass heating, special applications (brazing, banding, sealing, coating), melting, and welding. Brazing induction is a complex process involving electromagnetism, materials science, heat transfer and circuit analysis. It consists of a heating inductor (also known as induction coil), a power supply and a water cooling system, controls and the workpiece. It is suitable for high-volume production due to its speed and automation capabilities (Rudnev; Loveless and Cook, 2017).

In induction brazing, heating is achieved by the dissipation of heat generated by eddy currents. These currents are induced by a coil connected to an alternating current source. This method provides fast and concentrated heating, with the rest of the piece being heated through conduction (Zazycki *et al.*, 2017).

#### *2.1.7.1 Induction heating*

In 1831, Michael Faraday discovered that a changing magnetic field could induce a current in a wire without any contact and from this, began the studies about inductive heating. The principle of inductive heating consists of an alternating current (AC) flowing through a coil that can generate a magnetic field that varies with time, with a magnetic flux ( $\Phi$ ). When a piece is introduced into the magnetic field, an eddy current ( $I_k$ ) will be induced, having the same frequency as the current in the coil but in the opposite direction, as illustrated in Figure 3 (Peter, 2014; Rudnev; Loveless and Cook, 2017).

**Figure 3** – Principle of inductive heating

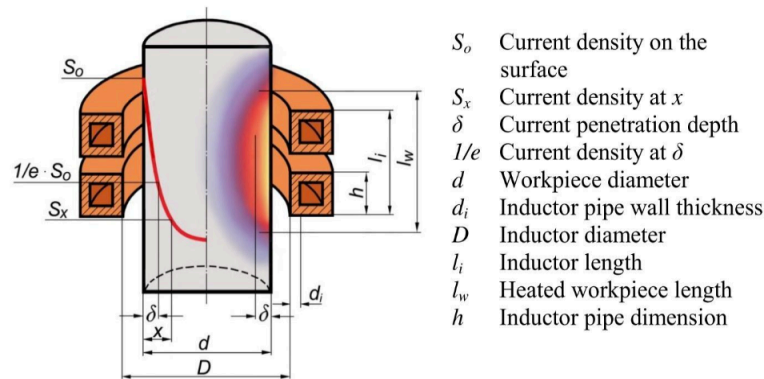


Source: Peter, 2014.

The induced current in the workpiece also generates a magnetic field, but in the opposite direction to the primary field. Both magnetic fields overlap, and there is a reduction in the radial direction of the total magnetic field. There are losses from the current ( $I_k$ ) due to the material's electrical resistance, following Joule's law ( $Q = I^2Rt$ ), and it causes the material to heat. The current density is related to the magnetic field strength, so as the magnetic field decreases from the outer edge towards the interior, so does the current density. As a consequence, the maximum current density is observed on the surface of the piece ( $S_0$ ) (Peter, 2014).

The phenomenon caused by the non-uniform current density is called skin effect, as it can be seen in Figure 4. This effect results in a concentration of eddy current on the surface of the workpiece, and the extent of this effect depends on the frequency, properties of the conductor, and the geometry of the workpiece (Rudnev; Loveless; Cook, 2017).

**Figure 4 – Current density distribution and heating**



Source: Peter, 2014.

Peter (2014) says that the current penetration depth ( $\delta$ ) is the depth at which the current density has decreased to 37% of its maximum value. On the piece axis, the current density is zero. The depth of current penetration can be determined by Equation 5.

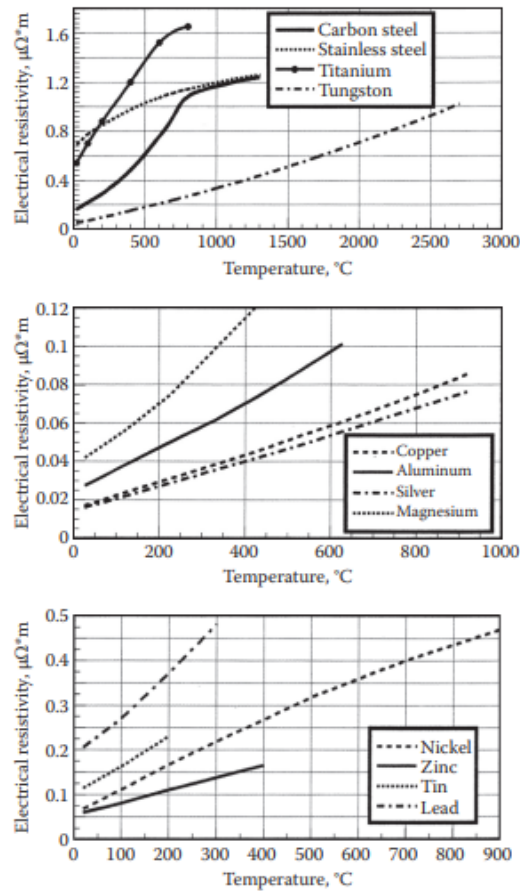
$$\delta = 503 \sqrt{\frac{\rho}{\mu_r X f}} \quad (5)$$

Considering  $\rho$  as the material's specific electrical resistance,  $\mu_r$  relative permeability and  $f$  the frequency.

From the equation, the current penetration depth decreases with increasing frequency and permeability, and decreases with decreasing specific electrical resistance. It is important to note that electrical resistance may increase during heating, making the current penetration depth also depending on the temperature. This relation means that the current penetration depth, i.e., the thickness of the heated layer, can be controlled by adjusting the frequency. Consequently, higher frequencies would result in reduced heating depth, while lower frequencies would result in increased heating depth (Peter, 2014; Rudnev; Loveless; Cook, 2017).

Electrical resistivity, or specific electrical resistance, is defined as the ability of a material to resist an electric current and it varies with temperature, chemical composition, microstructure, and grain size (Rudnev; Loveless and Cook, 2017). Figure 5 illustrates the electrical resistivity of some metals as a function of temperature.

**Figure 5** – Electrical resistivity of commercial metals



Source: Rudnev, Loveless and Cook, 2017.

The relative magnetic permeability is the material's ability to conduct magnetic flux compared to air and also affect current penetration depth. In the magnetization context materials can be classified into three groups: paramagnetic, diamagnetic, and ferromagnetic. For paramagnetic materials, the relative magnetic permeability is slightly higher than 1, while for diamagnetic materials it is slightly lower than 1. These two categories are also referred to as nonmagnetic materials since their difference in relative magnetic permeability is very small. Examples of nonmagnetic materials include aluminum, copper, titanium, and tungsten. In the case of ferromagnetic materials, they have a high value of relative magnetic permeability, for example iron and nickel (Rudnev; Loveless; Cook, 2017).

### 2.1.7.2 Process parameters

The factors influencing the brazing process can be classified into four main categories for better understanding: surface preparation, joint characteristics, material properties, and process parameters. Table 1 summarizes these categories. The parameters related to surface preparation, joint characteristics, and material properties have already been discussed in the previous sections.

**Table 1 – Brazing parameters**

Surface Preparation	Joint Characteristics	Materials Properties	Process Parameters
<ul style="list-style-type: none"> <li>● Presence of impurities (surface cleanness)</li> <li>● Flux application for oxide prevention</li> </ul>	<ul style="list-style-type: none"> <li>● Joint gap</li> <li>● Capillary action properties</li> </ul>	<ul style="list-style-type: none"> <li>● Melting point</li> <li>● Specific electrical resistance</li> <li>● Relative electric permeability</li> <li>● Filler-base material compatibility</li> <li>● Filler spreading capacity</li> </ul>	<ul style="list-style-type: none"> <li>● Current frequency</li> <li>● Power</li> <li>● Time</li> <li>● Inductor shapes</li> </ul>

Source: Way; Willingham and Goodall (2019); Peter (2014); Rudnev; Loveless and Cook (2017); Haus (2008).

In induction heating, the current frequency can vary from 50 Hz up to 27 MHz. For brazing, it ranges between 10 to 27 kHz (low frequency) for solid parts and 150 to 450 kHz (high frequency) for small parts. Lower frequencies increase the current penetration depth, which in turn increases the depth of heating, making them suitable for thicker parts. Higher frequencies are better for thin parts as they provide better heat distribution, allowing for more precise control over the heating process (Haus, 2008; Peter, 2014).

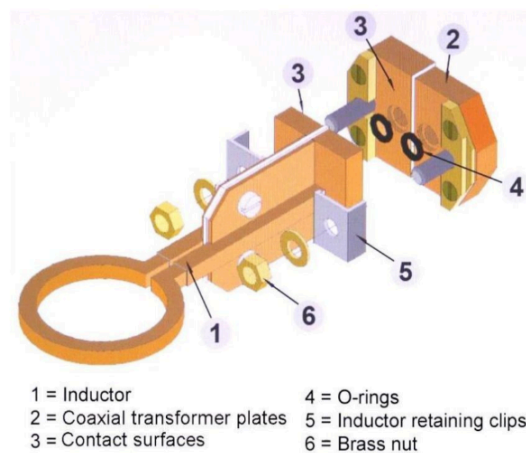
Power also plays a key role, because it controls the amount of energy transferred to the piece, together with time. Power levels can range from a few watts to several megawatts and to reach the necessary temperature for brazing, the heating time needs to be carefully considered. Induction brazing provides high power density, allowing the required brazing temperature to be reached very quickly. However, prolonged heating can damage components, while insufficient heating time can lead to inadequate brazing. Shorter heating times result in



lower heating losses, so achieving uniform heating of the workpiece requires a balance between time and power (Peter, 2014; Róžański; Rękasowski 2012).

The inductor is a crucial element because it transmits energy from the generator to the workpiece. Although an inductor is often referred to as a coil, it can have different shapes beyond the classic circular form. The design of the inductor depends on the application and specific process requirements, but when designing the inductor, the required energy amount is an important factor. Inductors are typically made with copper tubes that contain cooling channels, which are important for ensuring stability, efficiency, and a long service life. The jaws are made from solid copper. Inductor foot fittings are adaptable to various inductor shapes, and O-rings prevent water leaks that could affect cooling. The shape of the inductor is determined by the geometry of the workpiece (Haus, 2008; Peter, 2014). Figure 6 illustrates the detailed components of an inductor.

**Figure 6** – Exploded view of an inductor

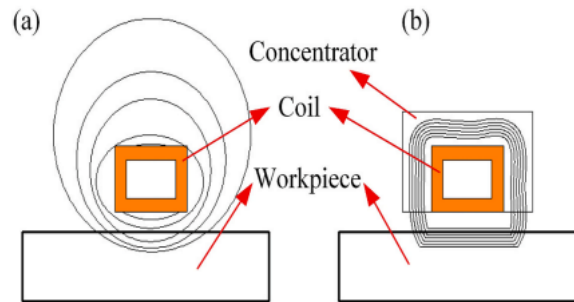


Source: Peter, 2014.

The magnetic flux from the coil is normally distributed in an even way, as it is seen in the lines around the coil in Figure 7a, and only a small part of the heat penetrates the material. To increase the flux in the direction of the workpiece, and therefore, heat efficiency, magnetic field concentrators, normally made of ferromagnetic metal powder can be used. They have higher magnetic permeability than the coil and can change the distribution of the flux, making it go in a localized area (Figure 7b), and also reduce the demand of current from

the coil, reducing losses. But from the other side, they can generate a combination of fields, making the process difficult to control (Wen *et al.*, 2021; Li *et al.*, 2012).

**Figure 7** – Magnetic field a) without and b) with field concentrators



Source: Wen *et al.*, 2021.

As described so far, in normal induction brazing the penetration depth depends mainly on frequency, where lower frequencies would result in smaller skin effects, but would lead to poor efficiency. With Vauquadrat penetration depth induction, even with low frequencies, effective penetration depth can be achieved (Moschinger, Vauderwange and Enzinger, 2024).

### 2.1.8 Brazing defects

According to Way, Willingham, and Goodall (2019), brazed joints can have defects in two main categories: joint formation and service. Defects from joint formation can be porosity and voids. Porosity has spherical geometry and is a consequence of trap gasses, and voids can have different shapes and result from various contaminants. Other motives for voids include excessive clearances, insufficient filler metal, insufficient temperature, and movement of the parts due to improper fixing. These defects can reduce the joint strength and can later cause leakage. Another joint defect is the formation of intermetallic phases during heating, which can also lower the mechanical properties of the joint (Schwartz, 2003).

Service problems are categorized into mechanical and corrosion. Bad design of the joint, for example, with sharp corners, improper joint clearance, and complicated joint geometry, can cause failure. Cracks can also cause premature failures as they can act as stress concentration points. Corrosion is a crucial concern, as joining two different materials can create galvanic couples that accelerate corrosion (Way; Willingham and Goodall, 2019).

ISO 18279:2023 classifies brazing defects into six groups: (I) cracks; (II) cavities; (III) solid inclusions; (IV) bonding imperfections; (V) shape and size imperfections and (VI) miscellaneous imperfections. In addition to this classification, imperfections can be either external or internal. External imperfections include surface-breaking porosity, localized melting, residual flux, excessive filler material (where filler has spilled over and solidified onto the base metal), among others. The main internal imperfections are gas entrapment, solid inclusions, incomplete filling (incomplete penetration of the filler through the joint), lack of fusion, and excessive alloying between filler and base metal.

Limits for gas pore presence are established in this standard, with a maximum of 20% of the projected area for class B and a maximum of 5% for class A. For filling imperfections, the limits are set at 80% or more of the projected area for class B and 90% or more for class A (ISO 18279:2023).

## 2.2 ALUMINUM ALLOYS

Aluminum is one of the most abundant elements on Earth, with a low density of 2.70 g/cm<sup>3</sup>, a melting point of 660°C, and a purity of 99% or higher. It has superior formability compared to materials with hexagonal structures, due to its face-centered cubic crystal structure, present in magnesium, for example, thanks to numerous slip systems. It is known for its lightweight, specific strength, and corrosion resistance, aluminum and its alloys are economically viable and great choices across diverse industries, especially in applications where reduced weight is required, like aircraft and automotive components (Çam and İpekoğlu, 2016; Kaufman, 2000).

Aluminum alloys are composed of two or more elements, which one or more are added to provide specific properties, and smaller amounts of other elements to modify fabrication properties. Common alloying elements used in aluminum include copper, magnesium, silicon, manganese, and zinc. Aluminum alloys can be classified into wrought and cast alloys. The Aluminum Association employs a designation system outlined by ANSI H35.1, consisting of four digits for wrought alloys. The first indicates the major alloying element, the second represents the variations in alloying elements within the base alloy, and the third and fourth represent specific alloys (Kaufman, 2000). Table 2 shows the corresponding element to each number in the first digit for wrought alloys.

**Table 2** – Main alloying elements in the wrought alloy designation system

Alloy	Main alloying element
1xxx	Mostly pure aluminum
2xxx	Copper
3xxx	Manganese
4xxx	Silicon
5xxx	Magnesium
6xxx	Magnesium and silicon
7xxx	Zinc
8xxx	Other elements (e.g., iron or tin)
9xxx	Unassigned

Source: ANSI, 2017.

The weldability of aluminum faces a lot of challenges, including the presence of a tenacious oxide layer, high thermal conductivity, distinct thermal expansion coefficient, and evolving melting characteristics. The formation of an oxide layer happens immediately upon exposure of aluminum to air; if not removed, it can compromise ductility and potentially lead to weld cracking. Due to its high thermal conductivity, aluminum alloys dissipate heat rapidly, requiring a faster heating rate to achieve elevated temperatures. The expansion coefficient for aluminum alloys is twice that of steel, posing a risk of crack formation; therefore, the heating rate must be carefully controlled (Çam; İpekoğlu, 2016).

### 2.2.1 Aluminum Solidification

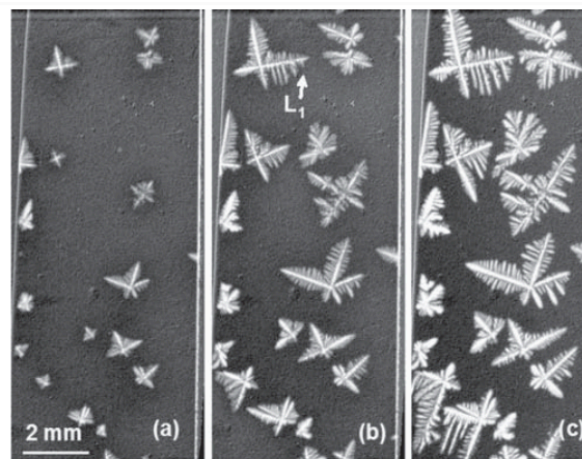
The phase transformation of a material from liquid to solid state can be explained using phase diagrams, which provide information about the phases formed, their quantities, the temperatures they are formed, and their compositions. A boundary, called liquid-solid interface, is formed by this transition and separates these two phases. In a two-component system, the temperature at which an alloy solidifies can change. For example, in aluminum,

the addition of a second element, such as silicon, normally decreases the melting point (Sigworth, 2014; Sobral, 2021).

During the solidification of liquid aluminum, small nuclei of solid metal are formed at the solid-liquid interface and grow into the liquid. The microstructure formed at this interface depends on the solidification rate, the thermal gradient, and the composition of the alloy. As the solute concentration increases or the solidification rate increases, the solute is expelled from the solid matrix, because its solubility in the aluminum matrix is limited. Once this limit is reached, solute atoms begin to accumulate in front of the solidifying crystal, this process is known as solute segregation (Sigworth, 2014; Sobral, 2021).

The rejection of solute, combined with local variations in composition, promotes a phenomenon called constitutional supercooling, where regions of the liquid near the interface have temperatures below the liquidus temperature. This undercooling creates conditions that destabilize the solidification front, encouraging the formation of dendrites (Ferrarini, 2005). The nuclei continue to grow until they meet neighboring grains, after which they can only increase in thickness and branch out in the structure. The structures formed during this process are called dendrites, which look similar to tree branches, as the ones in Figure 8, and occur only in alloys, not in pure metals (Sigworth, 2014; Sobral, 2021).

**Figure 8 – Dendrites in Al-20% Cu Liquid**



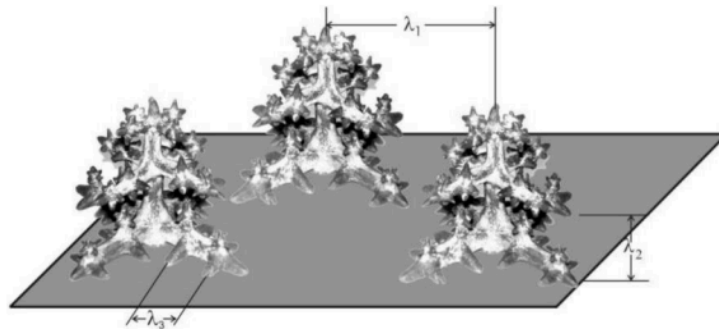
Source: Sigworth, 2014.

The formation of a dendritic structure is influenced by crystallographic factors, that means when the direction of growth is established, the structure begins to grow in other

directions, forming secondary and tertiary arms or branches, as Figure 9 shows (Sobral, 2021). The distances between dendrite centers and dendritic arms are known as arm spacings. Primary dendrite arm spacing ( $\lambda_1$ ) refers to the initial spacing between main dendritic trunks, secondary spacing ( $\lambda_2$ ) measures the distance between branches off the main trunks, and tertiary ( $\lambda_3$ ) spacing captures finer branches off the secondary arms (Dias Filho *et al.*, 2015).

The cooling rate directly affects dendrite formation during solidification. Higher cooling rates lead to finer dendrites with smaller spacings due to rapid solidification and limited solute diffusion, while lower cooling rates result in coarser dendrites with larger spacings. Dendrite arm spacing (DAS) influences material properties, with smaller spacings generally improving strength and reducing porosity but potentially increasing brittleness. Controlling cooling rates helps tailor microstructures for desired performance (Sobral, 2021).

**Figure 9** – Dendrites arms, primary  $\lambda_1$ , secondary  $\lambda_2$  and tertiary  $\lambda_3$  arm spacings



Source: Sobral, 2021.

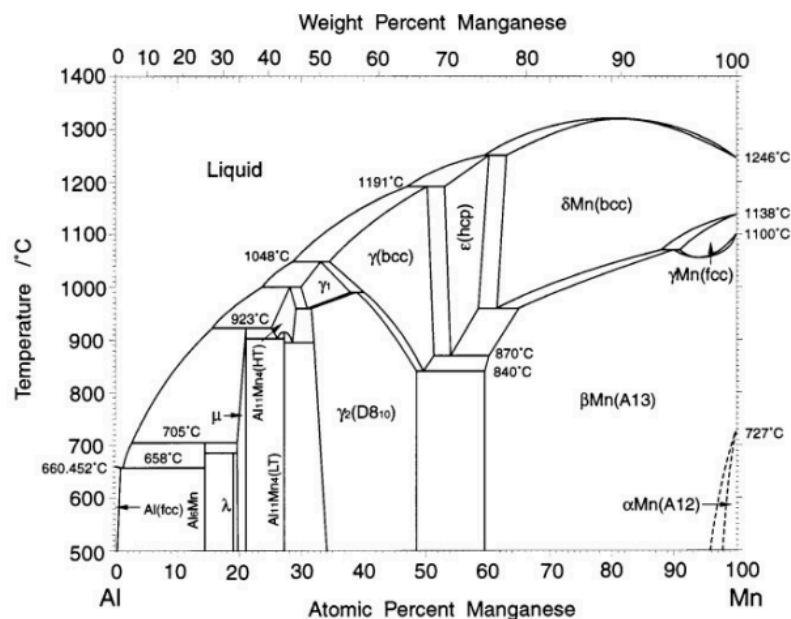
### 2.2.2 3XXX series

Alloys from the 3XXX series have manganese as the main alloying element, with typical concentration of manganese ranging 0.5 - 1.5%, and additions of Fe and Si (Engler; Brüggemann and Hasenclever, 2021). 3XXX series are renowned for weldability and recognized as the optimal choice among aluminum alloys for brazing and soldering, such as 3103 and 3003 (Kaufman, 2000). They are frequently used in the automotive industry for heat exchangers due to their low density, good corrosion resistance and thermal properties and usually in the form of extruded tubes or bars, joined by brazing or cladded films (Lanzutti; Andreatta; Magnan and Fedrizzi, 2018). Other applications for 3XXX alloys include packaging, building and home appliances.

Manganese contributes significantly to enhanced formability, ductility, and corrosion resistance in diverse environments. It also assures a fine grain size to the alloy and increases mechanical strength and hardness by solid solution hardening and dispersoid hardening (Moema; Siyasiya; Morudu and Buthelezi, 2023; Raji and Oluwole, 2012).

The aluminum-manganese phase diagram can give an idea of composition and microstructure. This diagram can be seen in Figure 10 and shows the precipitation of Al<sub>6</sub>Mn in the re-heating process, with eutectic reaction around 660°C and 1,9% Mn (Silva Junior, 2020, Shen; Hu; Liu e Hu, 2023). These alloys have low solubility of Mn, therefore they are normally in a supersaturated condition in the aluminum matrix. Additions of Fe and Si decrease even more Mn solubility in Al (Engler; Brüggemann and Hasenclever, 2021). The supersaturation is reduced by the formation of precipitates, also called dispersoids. The dispersoids can be found as two forms orthorhombic (Mn, Fe)Al<sub>6</sub> and cubic (Fe, Mn)SiAl<sub>12</sub> for higher concentration of Si (Calçada, 2018).

**Figure 10** – Phase diagram of Al and Mn

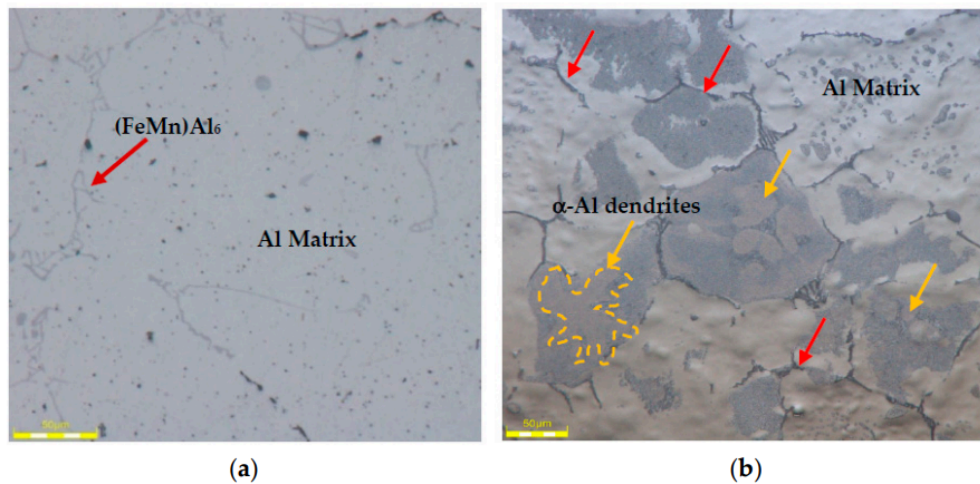


Source: Silva Junior, 2020.

The 3XXX series as-cast microstructure consists of aluminum dendrites and intermetallic particles, on the grain boundaries or interdendritic region (Du, Poole, Wells and Parson, 2013). For coarse dendrites, the dispersoids are more concentrated in the periphery than in the center region (Moema; Siyasiya; Morudu and Buthelezi, 2023). This

microstructure is indicated in Figure 11, where aluminum dendrites are indicated by yellow arrows while the dispersoids are pointed in the red arrows. This is a typical eutectic constituent appearance. The size and morphology of the dispersoids will affect ductility and formability of the alloy. This can be changed by homogenization processes, such as annealing. After homogenization, the arrangement is similar, but the volume of dispersoids is smaller and more rounded (Engler; Brüggemann and Hasenclever, 2021).

**Figure 11** – 3003 alloy a) polished and b) etched

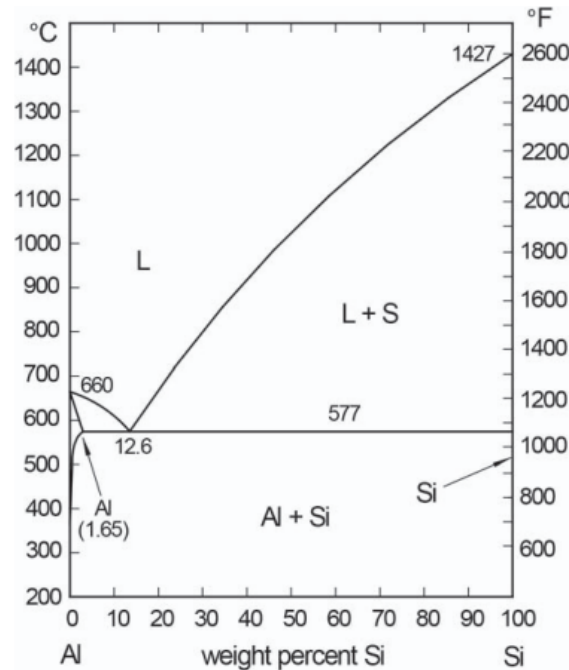


Source: Moema, Siyasiya, Morudu and Buthelezi, 2023.

### 2.2.3 4XXX series

4XXX series alloys are based on aluminum and silicon, with 7 to 14% Si. These alloys have good fluidity and a low thermal expansion coefficient, which makes them suitable for brazing fillers. The eutectic point is around 12.6% Si at 577°C, Figure 12 shows the phase diagram of Al-Si. Addition of silicon tends to increase the hardness and tensile strength of the alloy (Kakitani, 2021). Silicon also decreases the melting point of aluminum, increasing the alloy's suitability for brazing. The eutectic alloy typically contains between 10 to 13% silicon. However, there are also hypoeutectic alloys with silicon concentrations from 5 to 10% and hypereutectic alloys with 15 to 20% silicon (Sigworth, 2014).



**Figure 12** – Phase diagram of Al and Si

Source: Sigworth, 2014.

The microstructure of these alloys consists primarily of dendrites of  $\alpha$ -Al and Si in the eutectic region. Dendrite formation is often observed even in eutectic compositions, because there is a competitive relationship between the formation of primary phase and the eutectic, so the phase that develops at a higher rate exhibits preferential growth. From this, the primary phase can be formed instead of the eutectic, in certain conditions, even in alloys that are eutectic in nature (Kakitani, 2021).

Besides Si's power to increase tensile strength, the resistance is also affected by the dendrites, the refinement of dendrites can increase the tensile strength (Kakitani, 2021). In the eutectic region, the Si structure is in the form of needles, and therefore it acts as concentration points. Modifying elements such as Na, Sr, and Sb can transform Si needles into more fibrous or globular forms, increasing strength (Hosch and Napolitano, 2010).

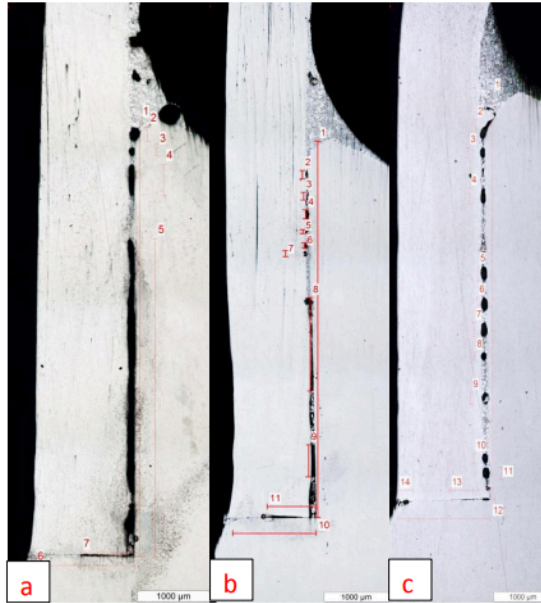
For the chemical properties, Al and Si form galvanic pairs, with Si being the cathode and Al the anode, leading to the corrosion of Al, especially in the eutectic region (Kakitani, 2021). Corrosion typically occurs in the grain boundary/interdendritic region, as these areas contain more intermetallic compounds. Some studies have shown that coarser dendritic structures have better corrosion resistance than finer ones because finer dendrites have a greater number of boundaries and are more susceptible to corrosion (Gomes *et al.*, 2021).

### 2.2.4 Aluminum Brazing

Aluminum brazing is a preferred technique for joining heat exchanger tubes due to its ability to join different components at the same time that it provides precise control of temperature, which is critical for aluminum. Al-Si filler alloys are the most commonly used materials for heat exchangers. In the study by Zhao, Elbel and Hrnjak (2021) two base alloys were used for brazing tests: AA3003 and AA6061; and two types of filler alloys: Al12Si and Zn15Al, having in total four combinations of brazed joints. Brazing was conducted in a furnace and the Zn-Al filler required smaller temperatures than the Al-Si filler. A "sessile drop test" was performed to verify the wetting contact angle, with assistance of a 3D scanning microscope. It was seen that Zn15Al filler metal showed good wettability on the AA3003 base metal, that means, the wetting contact angle is smaller than  $90^\circ$ . For the Al12Si filler, wetting was higher on the AA3003 metal. With increasing Mg content, wettability decreased, leading to lower wettability on AA6061.

In Vozniaki's (2014) study, it was compared the difference in filling and metallurgical characteristics of aluminum components brazed with three different brazing fillers. A flange was brazed to a tube with a Filalu 1192 ring with intern flux, an AlSi12 ring with external flux addition and NPA 1070-400 paste. The tubes were made of a 3xxx series alloy, and the flanges were made of 6XXX series alloy. Figure 13 shows the filling behavior of the three joints, and it is possible to see that filling is mainly at the top of the joint, near the ring.

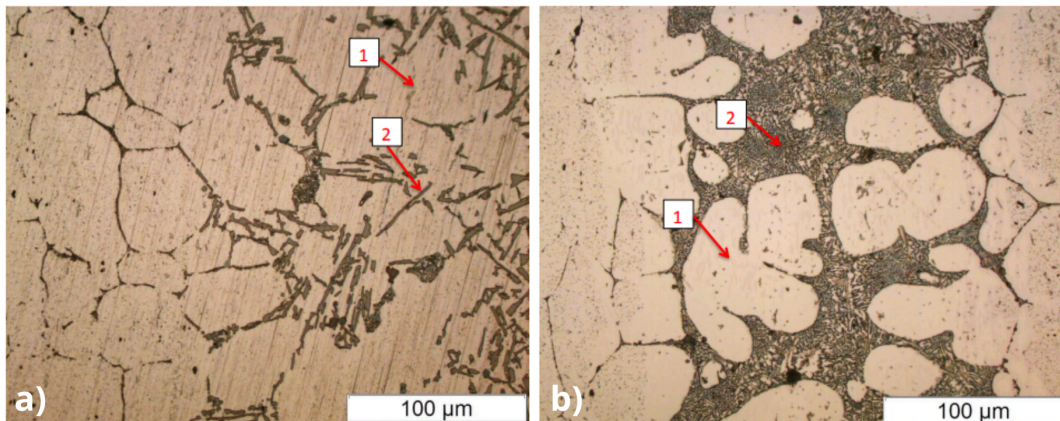
**Figure 13** – Filling of the joint with a) ring without intern flux, b) ring with intern flux and c) brazing paste



Source: Vozniaki, 2014.

The observed microstructure is shown Figure 14. The white phase in Figure 14a, indicated by the number '1', represents the Al- $\alpha$  matrix and the needle shaped phase indicated by the number '2' is eutectic Si. This microstructure was observed when brazing with Filalu and AlSi12. In the case of the brazing paste, the microstructure was different. Figure 14b shows a structure formed by dendritic arms with refined eutectic silicon.

**Figure 14** – Microstructure of brazed region with a) ring without intern flux and b) brazing paste



Source: Vozniaki, 2014.

The insights from these studies serve as a reference for understanding the results from aluminum brazing methods. However, the penetration depth induction technique, used in this work, distinguishes itself from normal induction brazing by employing controlled electromagnetic fields to achieve deeper and more uniform heating of the joint.

### 3 MATERIALS AND METHODS

The following sections describe the materials used, the processes, and the characterization techniques applied to achieve the objectives of this study.

#### 3.1 MATERIALS

The tubes used were made of the aluminum alloy 3103, supplied by Hydro, in the O/H111 temper. This temper means that the material was strain-hardened and partially annealed to obtain a balance between strength and formability. The alloy contains approximately Mn and Fe, as Table 3 shows, which contribute to its mechanical properties and corrosion resistance. Two types of tubes were used and their average dimensions are exposed in Table 4. The sleeves from the tubes were made with a tube expander tool, which cannot guarantee precise dimensions.

**Table 3** – Chemical composition of 3103 alloy

Element	Al	Si	Fe	Cu	Mn	Mg	Cr	Zn
Min %					0.9			
Max%		0.5	0.7	0.1	1.5	0.30	0.1	0.20

Source: Inspection/Test Certificate. Hydro. Order number: 4500028519, 2021.

**Table 4** – Average dimensions of the tube

Type	External diameter (sleeve)	Internal diameter (sleeve)	External diameter (tube)	Wall Thickness	Joint clearance
A	13.225	12.055	11.745	0.575	0.31
B	13.395	11.94	11.745	0.72	0.195

Source: the author, 2024.

For the filler material, Filalu 1192 was selected, which consists of a 4047A aluminum (composition shown in Table 5) alloy with FL20-B flux (based on potassium fluoroaluminate). The filler was supplied by Lucas Milhaupt in the form of pre-shaped rings. Figure 15a and b illustrates the assembly of the tubes. The flux was applied to the joint area before brazing. Magnetic field concentrators, Figure 15c, made of an amorphous iron-silicon alloy were used in some tests to direct the magnetic field to the workpiece. The active elements of the inductors were manufactured from pure copper by a third-party, using SLM-3D-printer and based on the drawings developed and presented in this work.

**Table 5** – Chemical composition of 4047Aalloy

Element	Al	Si	Cu	Fe	Mn	Mg	Ti	Zn	Cd	Pd	Other
Min %		11									
Max%		13	0.3	0.6	0.15	0.10	0.05	0.20	0.010	0.025	0.05

Source: Technical Data Sheet. LucasMilhaupt. FILALU 1192 NC / NCF / NCM, 2023.

**Figure 15** – a) Tubes, b) rings and c) field enhancers used



Source: the author, 2023.

## 3.2 METHODS

### 3.2.1 Flame brazing

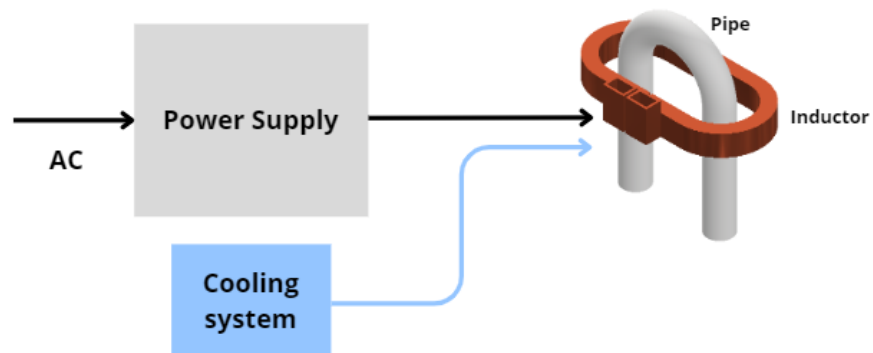
For comparison purposes, flame brazing was performed using an oxygen-propane torch. The process began by clearing the workspace of combustive materials to prevent accidents, then positioning the workpiece in a bench vise. The torch was prepared by adjusting the oxygen and propane valves to achieve the desired flame characteristics. Ignition was initiated with a spark. A blue flame, indicative of a high oxygen concentration and

elevated temperature, is too hot for aluminum brazing. Therefore, the oxygen content was reduced until an appropriate flame was achieved. Once the flame was regulated, it was passed evenly around the brazing region to ensure uniform heat distribution. As the brazing ring began to melt, the flame was removed from direct contact with the tube to prevent overheating.

### 3.2.2 Induction brazing

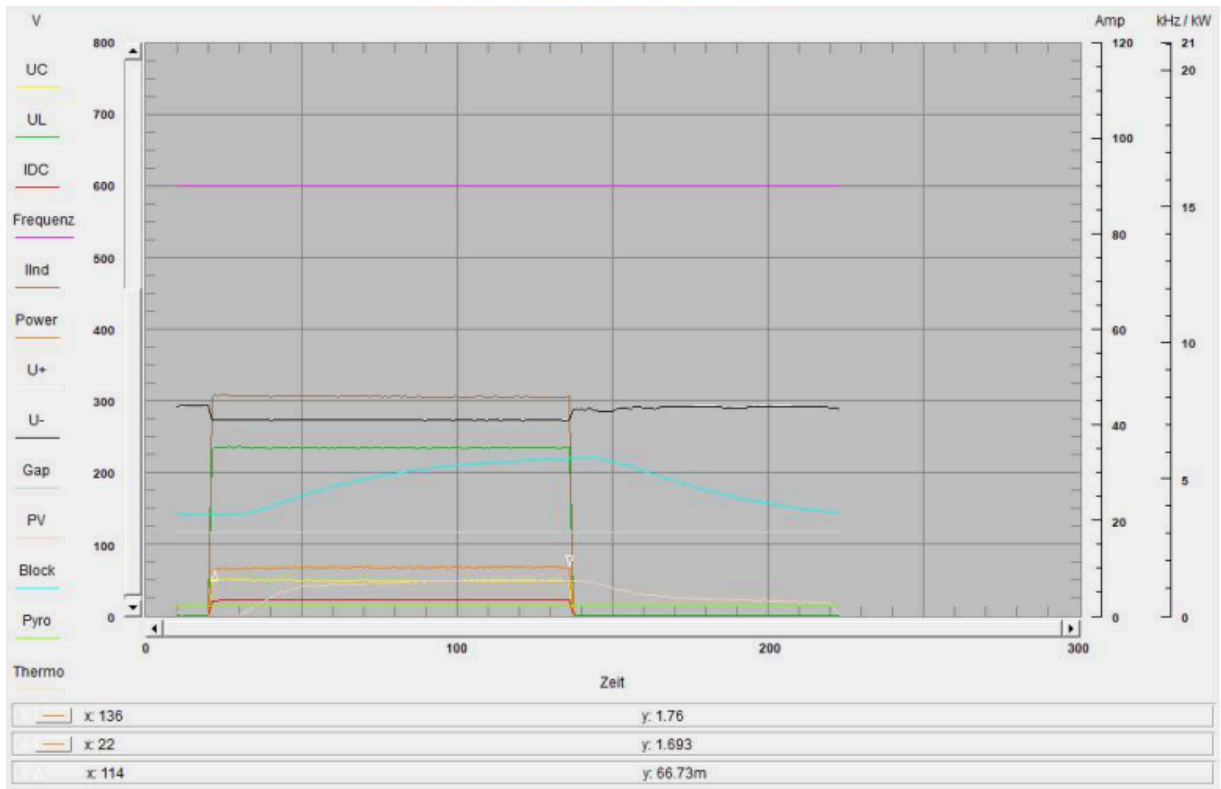
The induction brazing system consisted of a VauQuadrat V4 machine, an inductor, a cooling system, and the workpiece, as such in Figure 16. The parameters of the brazing process, such as frequency, pulse width modulation, power, and time, were controlled using dedicated software. Figure 17 shows an example of the graphical output from the software, illustrating the parameters from the beginning to the end of the process.

**Figure 16** – Schematic drawing of the induction brazing system



Source: the author, 2024.

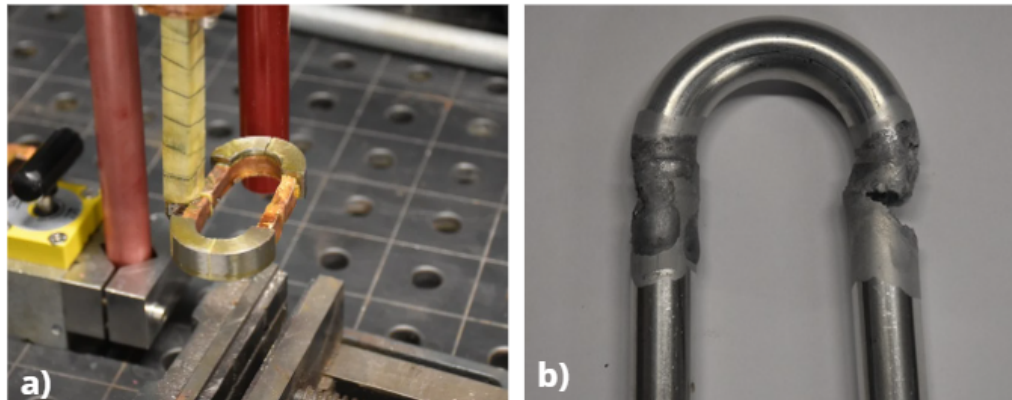
**Figure 17 – Software Output Over Time**



Source: the author, 2023.

For the initial tests, the frequency and pulse width modulation were kept constant, while the power was varied. Power measurements were taken using a power meter to ensure accuracy. Initially, an inductor fabricated manually, with field enhancers on the outer edges (Figure 18a), was used. The parameters used in the machine were a capacitor of 3  $\mu\text{F}$ , frequency of 15.8 kHz and a minimum gap of 8  $\mu\text{s}$  (or pulse width modulation, which regulates the amount of energy delivered to the system by varying the width of the current pulses) and the tubes were strategically positioned in a vertical orientation to make the most of gravity. It was seen that the tubes were heating up faster at the outer edges, leading to burning the aluminum and creating a hole (Figure 18b), 60% of power was used. Due to this, a new inductor design was developed.

**Figure 18** – a) Manually fabricated inductor and b) burned tube



Source: the author, 2023.

In this work, the terms 'one-step process' and 'two-step process' are used. A one-step process means that the power is maintained at the same level during the entire process. A two-step process begins with a higher power to accelerate the initial phase, which is maintained for a few seconds. The power is then reduced to prevent overheating as the filler material melts.

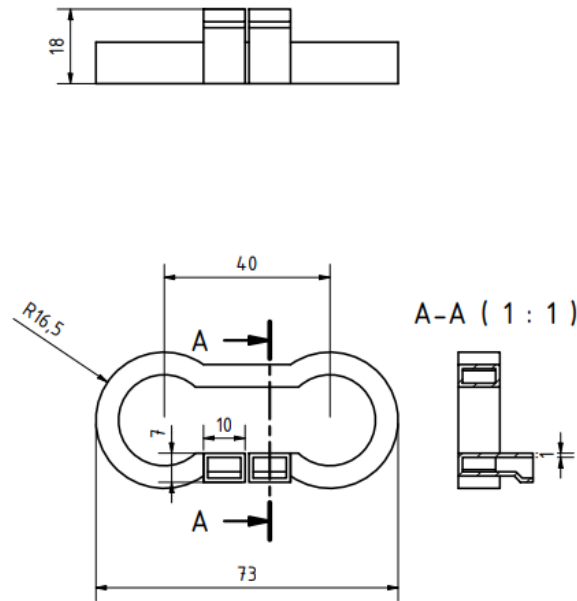
### 3.2.3 Development of inductors

The dimensions of the new inductor were similar to the one made manually, as is shown in Figure 19; however, it was made in a way that the inductor followed the curvature of the tube towards the inner part with a distance inductor-tube of 5 mm. The main part of the inductor was fabricated using 3D printing with pure copper and the connections were welded with TIG<sup>1</sup> (Figure 20a). The field concentrators were positioned close to the inner part of the tube, as can be seen in Figure 20b, because it is the less favorable region for heating. The 3D printed part of the inductor is called 4GYD32, and the finished inductor 2.NY 281.

<sup>1</sup> TIG is a welding process where parts are joined by the heat from an electric arc between a non-melting tungsten electrode and the workpiece, with a shielding gas protecting the area (Singh, Dey and Rai, 2017).

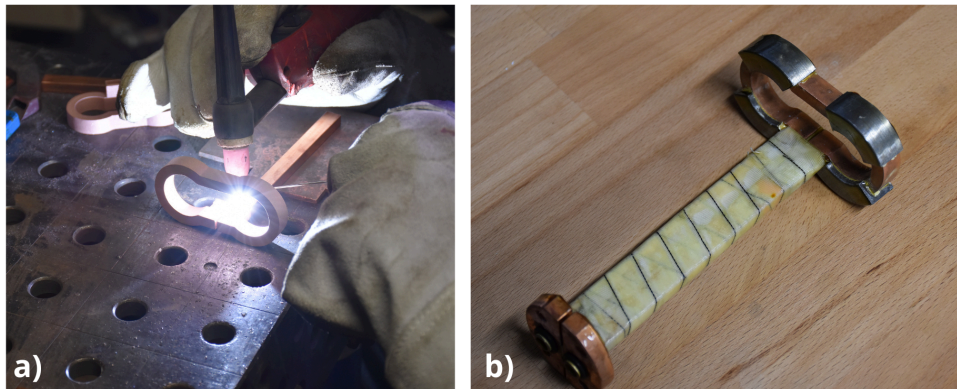


**Figure 19** – Technical drawing of the printed part of inductor - 4GYD32



Source: VauQuadrat, 2024.

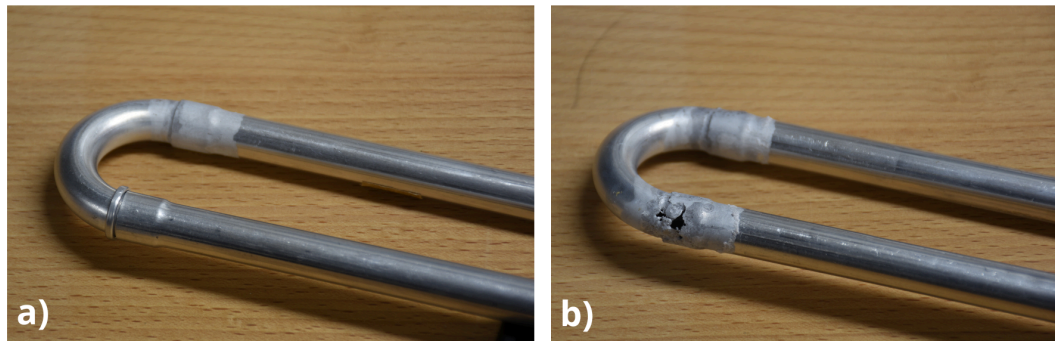
**Figure 20** – a) TIG welding and b) finished inductor



Source: the author, 2023.

With the new inductor, it was important to find the right capacitor to avoid damaging the machine, for that the current should be below 120A (going beyond this limit can lead to the machine's damage, although the specific reasons for this were not discovered yet). A  $6 \mu\text{F}$  capacitor was selected, with a frequency of 18.5 kHz and a minimum gap of  $9.5 \mu\text{s}$ . These parameters were good for the machine. However, it was observed that one side of the tube was always brazing before the other, resulting in either one side not being brazed while the other is (Figure 21a) or one side brazing while the other burned, opening a hole (Figure 21b).

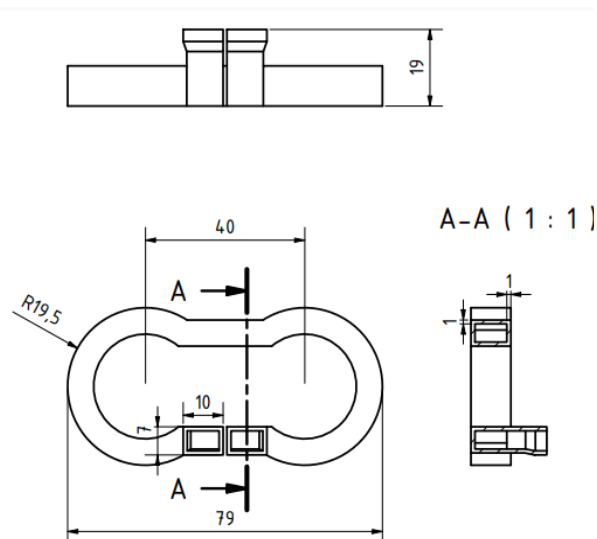
**Figure 21** – a) One side is not brazed while the other is and b) one side brazed while the other burns



Source: the author, 2024.

One possible reason for this effect is positioning of the field concentrators, which was made manually and can have a small variation from one side to the other, causing a difference in heating on both sides. An inductor without field enhancer was also tested, but the results were similar. Another factor to consider is the distance between the inductor and the tube; if this distance is too small, aluminum will be more susceptible to excessive heating. To correct this, another inductor with a greater distance was designed, expecting a more uniform and less critical heating process. The dimensions of the larger inductor are shown in Figure 22, and the distance between inductor and tube increased to 7 mm. The 3D printed part is referred to as 4GYD33, while the completed inductor is referred to as 2.NY 282.

**Figure 22** – Technical drawing of the printed part of inductor - 4GYD33

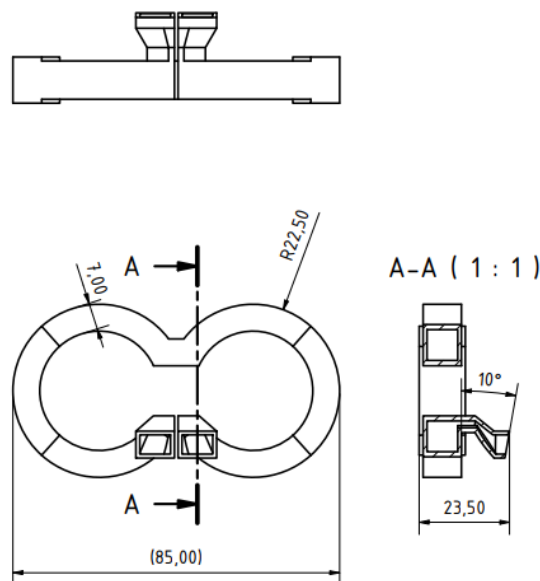


Source: VauQuadrat, 2024.

The parameters previously used with the inductor 2.NY 281 (6  $\mu\text{F}$ , 18.5 kHz and 9.5  $\mu\text{s}$ ) were also possible with the inductor 2.NY 282. However, the distance between the inductor and the tube increased, resulting in the increase of the amount of power required to melt the ring. Therefore, even with 100% power in the machine, there was not sufficient heating for brazing. To increase the power the frequency was decreased in 0.5 kHz steps, until it reached 15.8 kHz with 8 $\mu\text{s}$  of minimum gap, which is the standard for the machine.

With the inductor 2.NY 282 no big changes were observed, even with larger distance the heating was still non-homogenous. To decrease the concentrated heating in the external part of the inductor, a new inductor was designed, with a thicker wall on the outside, as shown in Figure 23. The thicker walls were intended to reduce power in this region, since it was heating more than on the inside. The shape of the inductor is more similar to the curvature of the tube, with an even larger distance between the tube and the inductor (9.5 mm). The 3D printed part is referred to as 4GYD36, while the finished inductor is referred to as 2.NY 287.

**Figure 23** – Technical drawing of the printed part of inductor - 4GYD36



Source: VauQuadrat, 2024.

The parameters used for 2.NY 287, Figure 24, were the same as those used for 2.NY 282 (6  $\mu\text{F}$ , 15.8 kHz and 8 $\mu\text{s}$  of minimum gap). Initial tests showed fine results, with a reduction of the concentrated heating on the external parts of the inductor and a more homogeneous heating. After that, the brazing started in the horizontal position, as it is the

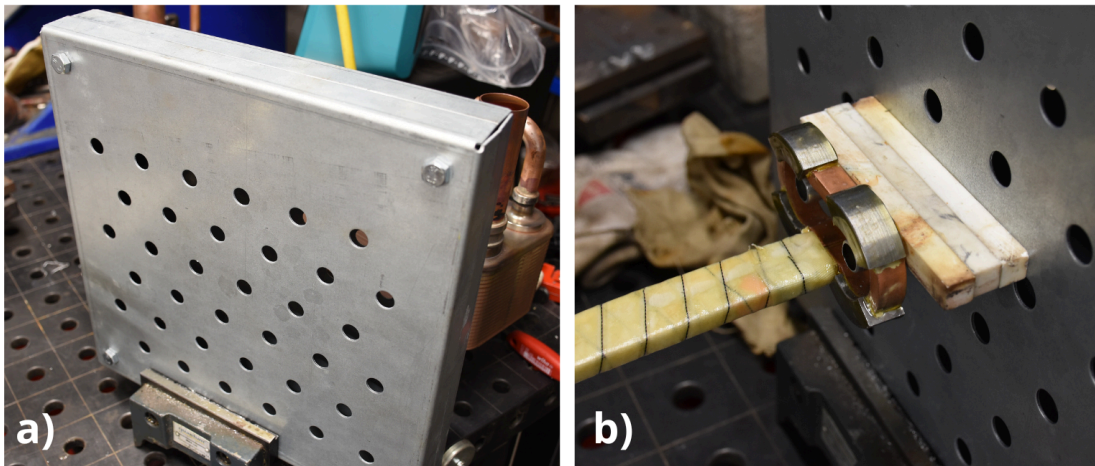
orientation that it will be used for future application in heat exchangers. A metal sheet with holes (Figure 25a) was used to ensure the tube's position, with three ceramic blocks (Figure 25b) to ensure the distance between the inductor and the sheet. A pachymeter and spirit level were used for alignment of the tube and inductor.

**Figure 24** – Finished 2.NY 287 inductor



Source: the author, 2023.

**Figure 25** – a) Metal sheet and b) ceramic blocks



Source: the author.

When the inductor, the process parameters and the setup were defined, the brazing process began with two power settings: 60% power, corresponding to 1.8 kW, and 100% power, equivalent to 5 kW. At 60% power, the process took nearly 2 min, but the brazing ring didn't fully melt. Using 100% power caused the tube to burn in just 16 seconds, showing that a power between 60% and 100% was needed. Brazing at 70% power (4.3 kW) took around 26

seconds but still resulted in burning. Reducing to 65% power (3kW) resulted in a successful brazing, but it took 49 seconds, which was considered too long for the intended application. The ideal time of the whole process would be less than 30 seconds.

To speed up the process, a two steps approach was introduced. The idea was to start the process with higher power for a small period and then reduce the power to a level where there was no risk of burning the tube. This two-step brazing process was programmed into the computer, with the time and power for each step. Initially, the first step started with 70% power for 10 seconds, and the second step was set with 65% power for 30 seconds to complete brazing but was manually stopped when the brazing ring melted, which started at 35 seconds and ended at 39 seconds for the tube A. Each trial was recorded with a camera to track the melting of the ring. Table 6 provides a summary of the power levels used and the respective times required for brazing.

Since 70% power for the first step resulted in 39 seconds of brazing, a further increase in the first step power was tried, reaching 80% and then 85%. The total brazing time decreased slightly, so an experiment was made by increasing the power of the second step to 67%. This proved to be risky, as the tube burned simultaneously with the melting of the ring. As a result, maintaining the power of the second step at 65%, for tube A, is best for a non-critical brazing.

To further reduce the total brazing time, the power for the first step was increased again. Additionally, an attempt was made to extend the time of the first step to 12 seconds, but no significant difference was observed. Next, the power was increased to 100%, resulting in a brazing time starting at 22 and ending at 25 seconds, without any risk of burning. Due to these findings, a configuration of 100% power for 10 seconds in the first step and 65% power for 30 seconds in the second step was considered optimal.

The parameters optimal for tube A resulted in a longer brazing time for tube B, which was from 39 to 47 seconds. This difference could be attributed to the fact that tube B is thicker than tube A. The heat transferred to the tube is also used to increase the temperature of the ring, meaning that the thicker tubes, more heating would be necessary. Given that, the power of the first step was already at 100%, an alternative was attempted by increasing the second step to 67%. This led to a reduction in the total time, and unlike tube A, it did not result in burning. However, increasing the power to 70% caused damage to the tube. Flux residues were not removed after brazing, due to its non-corrosive nature. Had the experiment

been continued, a better condition for tube B might have been found, but based on the current results, 100% for 10s and 67% for the remaining time was the best condition.

**Table 6 – Power settings and brazing time**

<b>Tube type</b>	<b>Power</b>	<b>Total brazing time</b>
A	60% (1.8 kW)	120s
A	65% (3 kW)	40s
A	70% (4.3 kW)	26s, but burned
A	100% (5 kW)	16s, burned
A	70% (4.3 kW) for 10s and 65% (3 kW) for 30s	35s to 39s
A	80% (4.9 kW) for 10s and 65% (3 kW) for 30s	28s to 33s
A	85% (4.9 kW) for 10s and 65% (3 kW) for 30s	30s to 34s
A	85% (4.9 kW) for 10s and 67% (3.5 kW) for 30s	22s to 35s, burned
A	90% (4.9 kW) for 10s and 65% (3 kW) for 30s	26s to 33s
A	85% (4.9 kW) for 12s and 65% (3 kW) for 30s	24s to 32s
A	100% (5 kW) for 10s and 65% (3 kW) for 30s	22s to 25s
B	100% (5 kW) for 10s and 65% (3 kW) for 30s	39s to 47s
B	100% (5 kW) for 10s and 67% (3.5 kW) for 50s	31s to 38s
B	100% (5 kW) for 10s and 70% (4.3 kW) for 50s	20s to 27s, but burned

Source: the author, 2024.

It is important to note that temperature measurements were not feasible during the experiments, limiting the ability to correlate specific thermal profiles with microstructural outcomes.

### 3.3 CHARACTERIZATION

#### 3.3.1 Samples preparation

The tubes were manually cut with a saw in the longitudinal section, to show the brazed joint, and then embedded in acrylic resin powder from Risitec, using self-curing acrylic liquid from Ideal Fast in a 1:2 ratio. After that, the samples were grounded with sandpaper from 80 to 2000 grit and polished with 1-micron diamond paste. Figure 26 shows an example of a sample with longitudinal view ready for metallographic analysis, each side of the sample was named with 'A' and 'B' to ensure reference during the analysis. Parameters such as power, time, type of tube and process are described in Table 7, with a 6 $\mu$  capacitor; 15.8 kHz for frequency and 8  $\mu$ s of minimum gap. For the one step process, only samples with 60 and 70% were tested to check the two extremes.

**Figure 26** – Sample prepared for microscopic analysis



Source: the author, 2024.

**Table 7** – Sample parameters

Sample Group	Brazing Process	Power - Time	Total time	Type of Tube
A	Induction	100% (5 kW) for 10s and 65% (3 kW) for 30s	22s to 25s	A
B	Induction	100% (5 kW) for 10s and 65% (3 kW) for 30s	39s to 47s	B
C	Flame	-	more than 1 min	A
D	Induction	90% (4.9 kW) for 10s and 65% (3 kW) for 30s	26s to 33s	A
E	Induction	70% (4.3 kW) for 10s and 65% (3 kW) for 30s	35s to 39s	A
F	Induction	70% (4.3 kW)	26s	A
G	Induction	60% (1.8 kW)	120s	A
H	Induction	100% (5 kW) for 10s and 67% (3,5kW) 50s	43s	B

Source: the author, 2024.

### **3.3.2 Visual inspection**

It was a simple and important method used to check if there were any defects present, like lack or excess of filler or heat, or bad alignment of the pieces. Visual inspection was conducted soon after the brazing process. Part of the visual inspection was made on the inner side of the brazed joint. For that some of the tubes were cut.

### **3.3.3 Optical Microscopy**

A Zeiss AxioLab.A1 reflected light microscope was used to inspect the microstructure and filling pattern of the samples. The analysis was conducted at the Microscopy and Structural Analysis Laboratory (LAMEA) of the Federal University of Santa Catarina (UFSC), in Blumenau.

### **3.3.4 Scanning Electron Microscopy and Energy Dispersive Spectroscopy**

The micrographs and elemental composition analyses were obtained using a Scanning Electron Microscope from the brand Tescan, model VEGA 4 LMS, coupled with an Energy Dispersive Spectroscopy (EDS) detector. The SEM was operated at an acceleration voltage of 25 keV, with a working distance (WD) of 18.83 mm and a magnification of 150x. Before the analysis, the samples were coated with a thin layer of gold using the sputtering method to ensure electrical conductivity and improve the quality of the images and EDS data.

### **3.3.5 Tensile test**

For the tensile test, a universal testing machine, Instron EMIC 23-100, located in the Mechanical Laboratory at UFSC - Blumenau, was used. The speed setting was 5 mm/min. The samples were different from those used for microscopy. Due to the shape of the tubes, it was not possible to fix them in the machine. Therefore, the samples were brazed using two straight tubes to create enough area for gripping, as shown in Figure 27.



**Figure 27** – Tensile test samples

Source: the author, 2023.

Since both ends of the tubes were open in this configuration, it required more power or time to complete the brazing process. As a result, different parameters were used, as shown in Table 8.

**Table 8** – Sample parameters for tensile test

Sample Group	Power - Time	Type of Tube
I	100%-10s 65%-120s	A
II	100%-10s 67%-120s	A
III	100%-10s 67%-120s	B
IV	100%-10s 70%-40s	A
V	Unbrazed	A

Source: the author, 2024.

From this test, it was possible to obtain tensile strength and strain values, as well as stress-strain curves. To calculate the stress, the tube area was based on an internal diameter of 10.21 mm and an external diameter of 11.745 mm, resulting in a cross-sectional area of 26.46 mm<sup>2</sup>. To estimate the joint strength, the area of the brazed joint was considered, using an internal diameter of 10.21 mm and an external diameter of 13.225 mm.

### 3.3.6. ANOVA

ANOVA (Analysis of Variance) was used to assess the statistical significance of differences in tensile strength and ductility among the various sample groups with the Software Minitab. The test compared the means of five distinct groups, each representing different brazing conditions, to determine if the variations in tensile strength and ductility were statistically significant. The null hypothesis assumed that there were no differences between the group means, while the alternative hypothesis suggested that at least one group mean was different.

A significance level of 95% was chosen, with a p-value of 0.05 serving as the threshold for statistical significance. The F-value was used to compare the variability between group means to the variability within groups. A higher F-value indicates a greater likelihood of significant differences among the means. The p-value was then evaluated: if it was less than or equal to 0.05, the null hypothesis was rejected, confirming that at least one group mean was significantly different. These criteria ensured that the analysis could reliably identify the impact of brazing conditions on tensile strength and ductility.

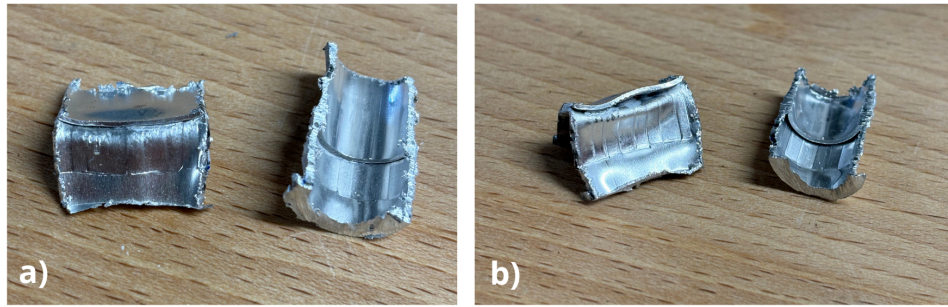
## **4 RESULTS AND DISCUSSION**

### **4.1 VISUAL INSPECTION**

The visual inspection was an important step during the development of a proper inductor, due to its help in identifying non-homogeneous heating or overheating. In the cases that excessive heating was visible, the design of the inductor was changed without the necessity of a microscope, similarly, when heating was insufficient to melt the ring, the design was also modified. This inspection also helped optimize brazing parameters. As shown before in Table 5, four samples were visibly burned due to overheating, while one sample lacked enough heat to melt the ring. For the remaining samples, no visible defects such as poor filler metal distribution, overheating of base material or partially melted filler metal were detected.

Two samples were selected for a more detailed visual inspection of the joint's inner section: one from group A and one from group B. Figure 28 shows these samples cut longitudinally. The gap between the two pieces, in Figure 28b, indicates poor attachment in sample B due to the incomplete filling. In the case of sample A, in Figure 28a, the gap between the two pieces appears to be completely filled.

**Figure 28** – Samples from a) group A and b) group B

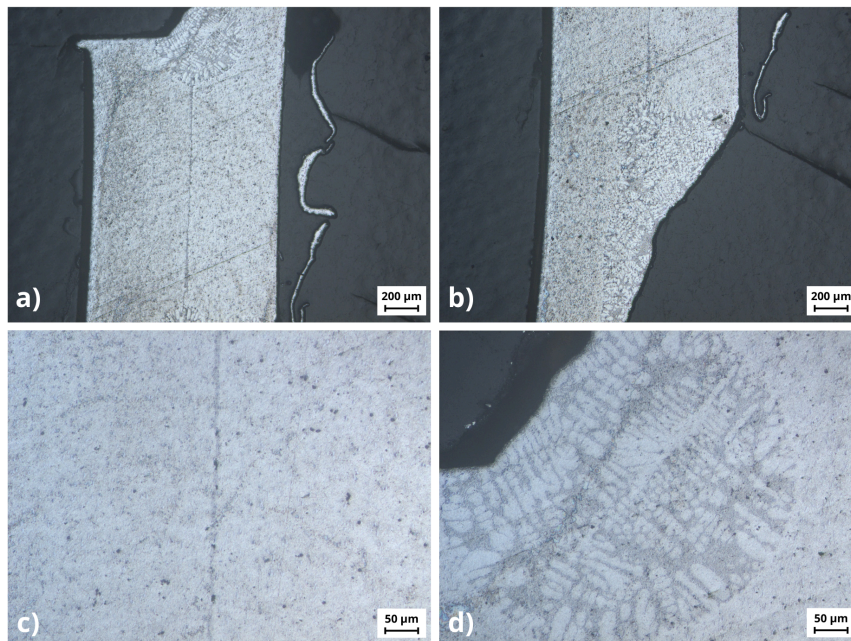


Source: the author, 2023.

#### 4.2 MICROSCOPY

Optical microscopy allows for the observation of the microstructure of the brazing alloy, providing insights into the filling process. In Figure 29, sample A1 shows a good filler distribution with no evidence of pores or voids. Dendrites are present, especially at the extremities of the brazed area. This dendritic morphology is typical of hypoeutectic alloys. At the center of the brazed region, where joint clearance is smaller and cooling is faster, a more refined eutectic structure is observed, which is normally thin and evenly distributed within the aluminum matrix, and the formation of more dendrites with small size (Chen *et al.*, 2014).

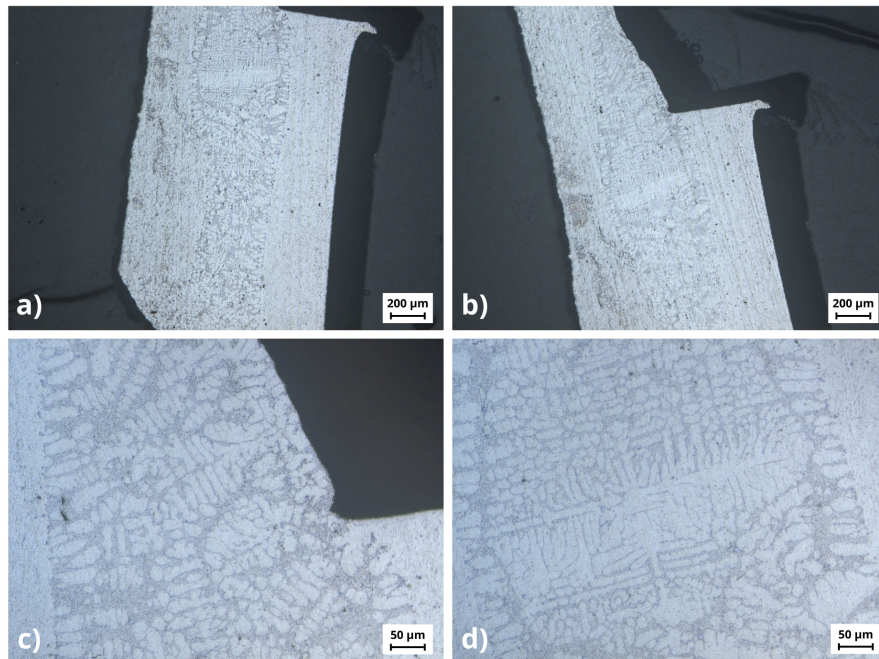
**Figure 29** – Microstructural analysis of sample A1 a) 50x of the overall joint; b) 50x of the upper side of the joint; c) 200x of the middle section; d) 200x of the lower part



Source: the author.

In Figure 30, sample A2 (from the same group as A1) shows the same morphology and filling pattern. Figure 30d shows a well-formed dendrite. There is an evident difference between the joint clearance of samples A1 and A2, likely due to the tube's lack of circularity. Some authors point out that dendritic microstructure may have higher amount of porosity than with the eutectic mode solidification, due to the fact that dendrites are formed by lower solidification rates (Kadhim, 2011). However, even with the presence of a dendritic microstructure in samples A1 and A2, no significant porosity was detected. This suggests that the solidification conditions in these samples, adequate joint clearance for example, were sufficient to prevent the formation of voids.

**Figure 30** – Microstructural analysis of Sample A2 a) 50x of the overall joint; b) 50x of the lower side of the joint; c) 200x of the lower part; d) 200x of dendrite

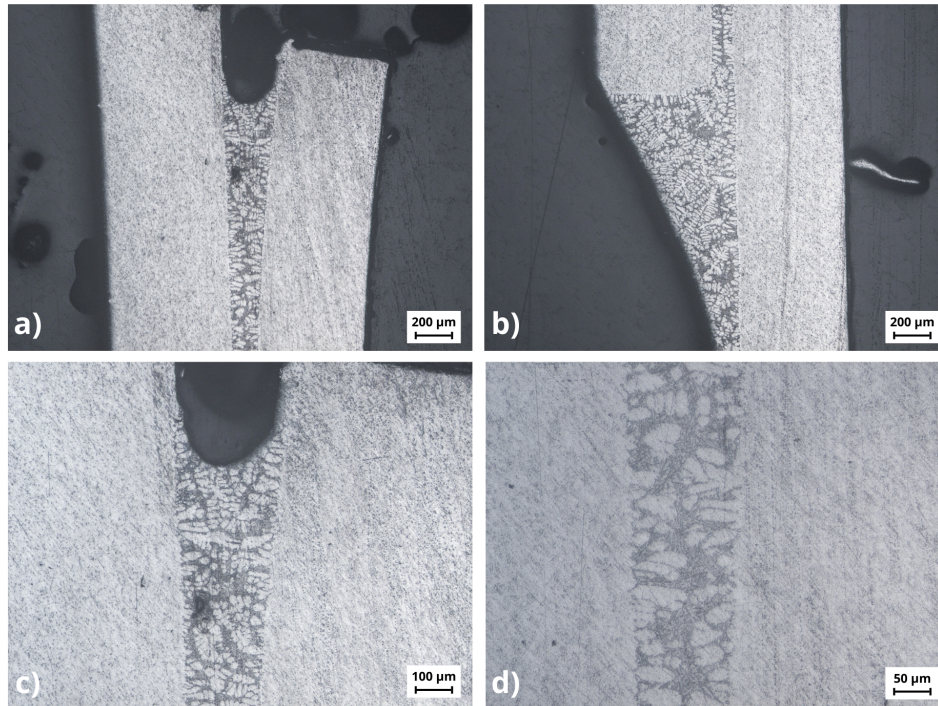


Source: the author, 2024.

Figure 31 illustrates sample B1, highlighting incomplete filling. Incomplete filling may lead to small fissures between the joined parts, allowing the accumulation of the refrigeration fluid into the interior of the tubes, which can result in corrosion over time. Even if initially, incomplete brazing does not lead to leakage, it may pose a potential risk to the long-term integrity and performance of the cooling system due to corrosion. Considering that aluminum exhibits negative electrode potential, it is even more susceptible to galvanic

corrosion. That is one of the reasons why filler alloys are normally made with Al and Si, Si does not enhance the corrosion (Jacobson and Humpston, 2005). Furthermore, sample B2 showed good filling with no apparent defects and the presence of dendrites.

**Figure 31** – Microstructural analysis of Sample B1 a) 50x of the lower side of the joint; b) 50x of the upper part; c) 100x of the lower part; d) 200x of the middle part



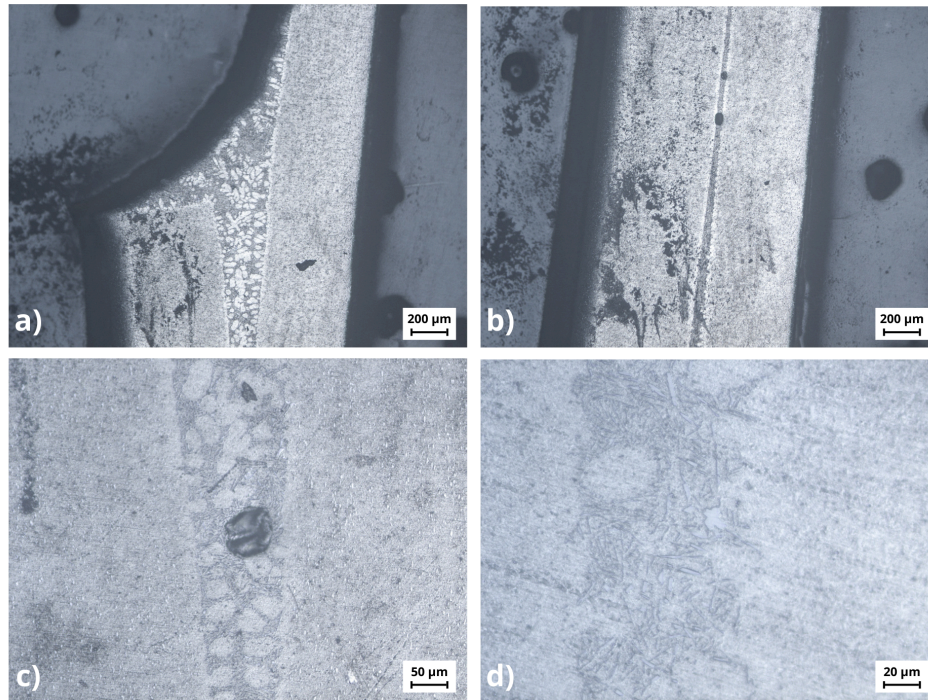
Source: the author, 2024.

Incomplete brazing may result from excessive joint clearance. The tubes used did not have perfect circularity, which may lead to areas where the joint clearance was too large to generate sufficient capillary pressure for complete filler penetration. Besides that, brazing time may have been insufficient, as the filler alloy begins to solidify as soon as heating ceases and it does not flow anymore, preventing it from going to the other extreme of the brazed region. The presence of dust and impurities can also contribute to the incomplete filling, as well as bad fixation of the tube.

Figure 32 shows sample C1, prepared by flame brazing, differing from the other samples. Visible defects are present, such as in Figure 32c, and eutectic silicon is more abundant, as shown in Figure 32d. The increase in eutectic silicon may correlate with the

different thermal profiles associated with flame brazing, which can lead to variations in cooling rates and microstructure.

**Figure 32** – Microstructural analysis of Sample C1 a) 50x of the upper side of the joint; b) 50x of the overall joint; c) 200x of the void; d) 500x

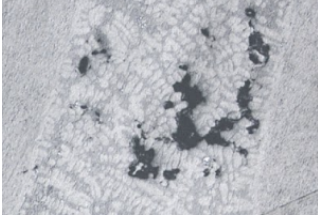
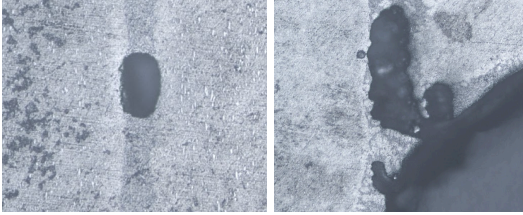
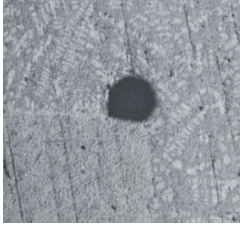

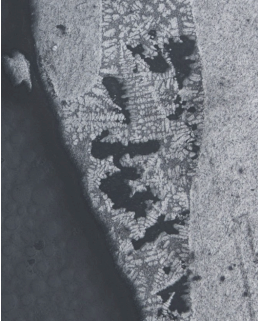


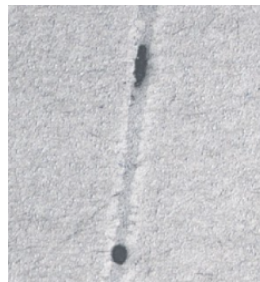
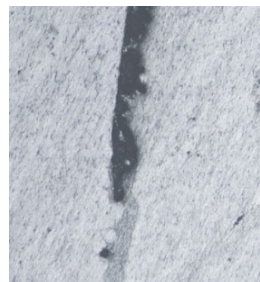
Source: the author, 2024.

Box 1 summarizes the filling pattern and defect occurrences across all samples. Samples A2, C1, F1 and F2 exhibit a type of porosity, likely caused by the contraction of the alloy during the solidification and insufficient filler metal feeding. Samples C1, E2 and G1 presented defects with spherical morphology, which are found normally in the interdendritic regions and caused by trapped gas (Dybowski *et al.*, 2016). Samples B1, F1, F2, G1, G2, H1 and H2 presented incomplete brazing. Groups F and G, which had lower heat inputs, are likely linked to this issue, while samples B1 and F showed incomplete brazing despite higher power settings and a two-step approach.

**Box 1** – Summary of filling characteristics and defect presence for each sample

Sample	Filling	Presence of defects
A1	Good	No

A2	Good	
B1	Incomplete	No
B2	Good	No
C1	Good	
D1	Good	No
D2	Good	No
E1	Good	No
E2	Good	
F1	Incomplete	
F2	Incomplete	

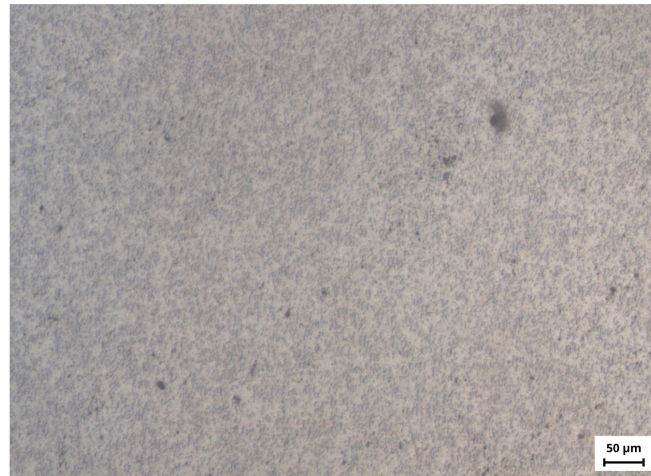
G1	Incomplete	
G2	Incomplete	
H1	Incomplete	No
H2	Incomplete	No

Source: the author, 2024.

The relationship between the presence of defects and the heat input during the brazing process is critical. Higher heat inputs typically enhance fluidity and penetration of the filler metal, whereas insufficient heat may result in incomplete filling. Figure 33 shows the microstructure of the filler metal before the application of heat, which is different from that seen after the brazing process, particularly due to the absence of dendrites. This suggests that there was likely some diffusion of aluminum from the base material into the filler metal, which altered the Al-Si alloy composition, bringing the silicon content to a hypoeutectic region and favoring the formation of dendrites. The diffusion between the base metal and the filler metal is a common phenomenon in brazing processes, and it can enhance the bond between the two materials (Way, Willingham, & Goodall, 2019).



**Figure 33** – Microscopy of the filler metal

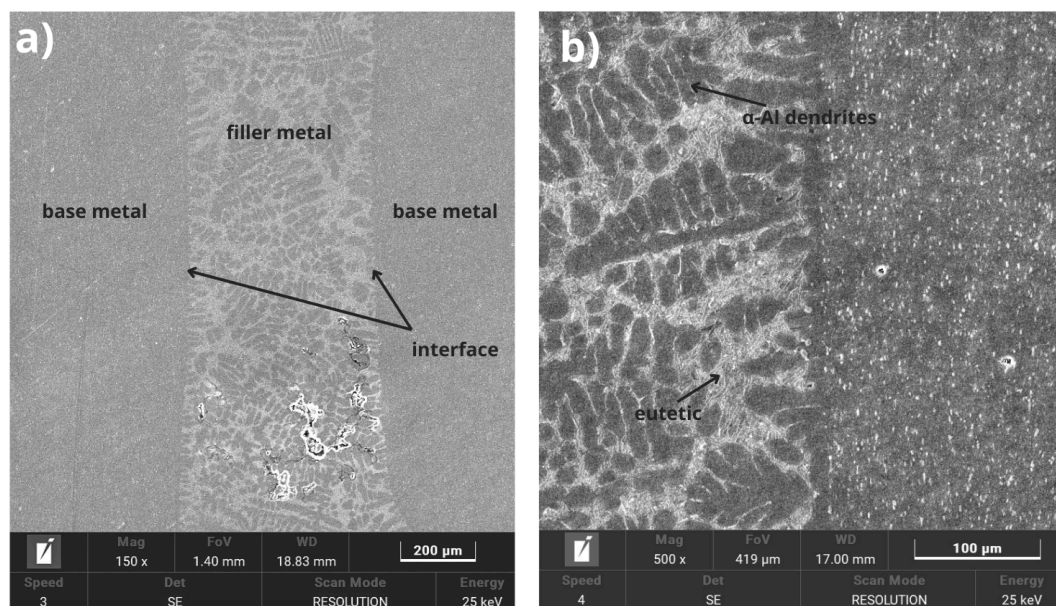


Source: the author, 2024.

#### 4.3 SEM – EDS

SEM imaging (Figure 34a) reveals the interface between the base and filler metals, with the porosity observed in optical microscopy also visible. Figure 34b shows the solidification front between the base and filler alloys, with solute segregation leading to an aluminum-rich interface.

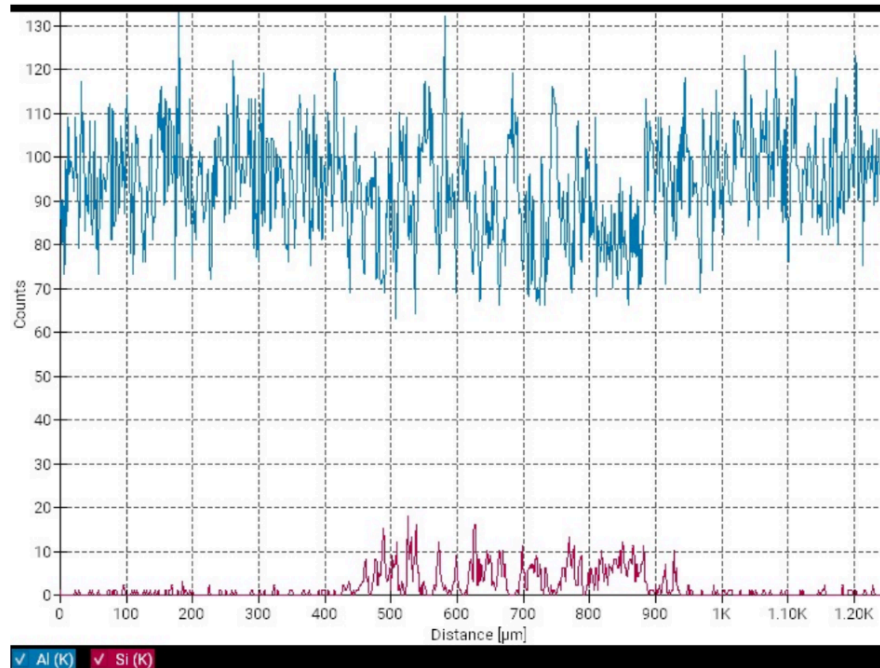
**Figure 34** – SEM images of sample A2 a) 150x and b) 500x



Source: the author, 2024.

EDS analysis of sample A2 (Figure 35) detected aluminum and silicon, with a higher concentration of silicon in the center of the joint, where the Al-Si alloy is located.

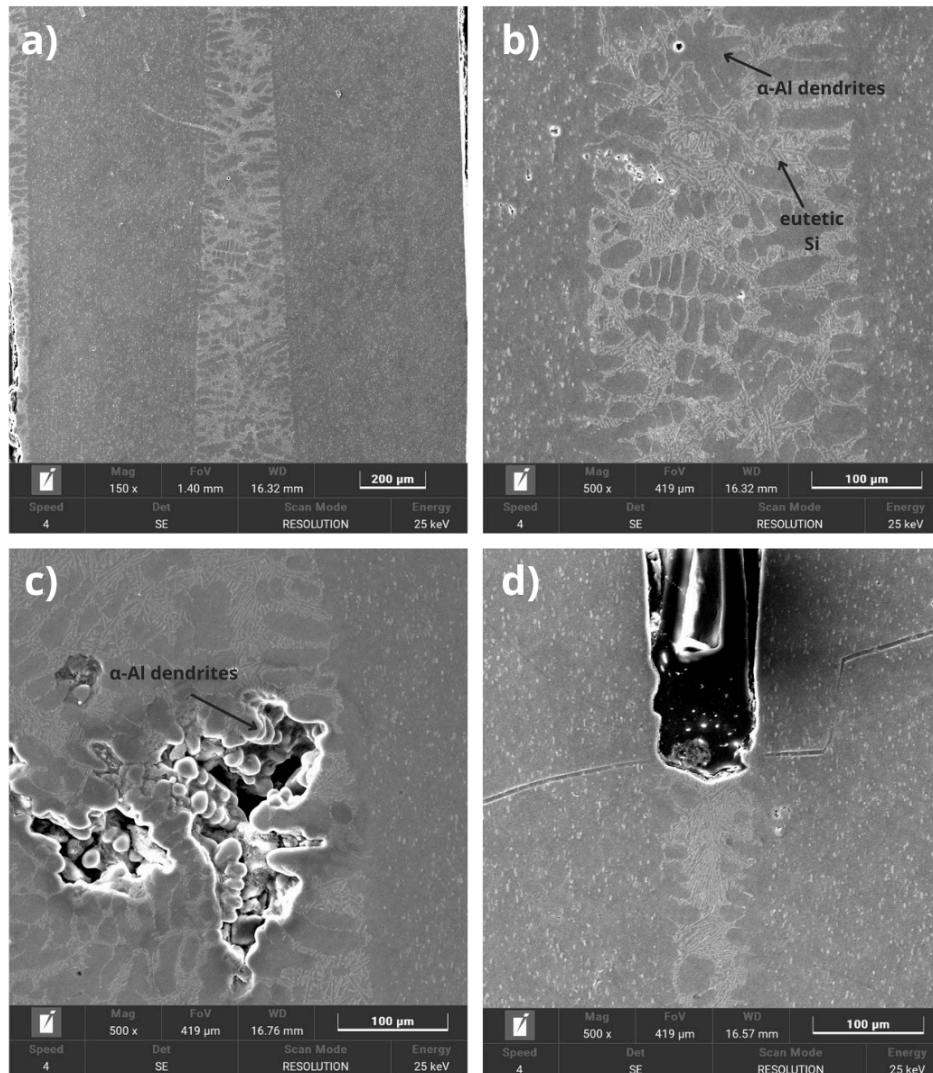
**Figure 35** – EDS of sample A2



Source: the author, 2024.

In Figure 36, for sample F2, the primary  $\alpha$ -Al dendrites with surrounding Al-Si eutectic are more evident. The Si eutectic appears as the white regions. The porosity observed in optical microscopy was captured with SEM, notably showing the dendritic arms.

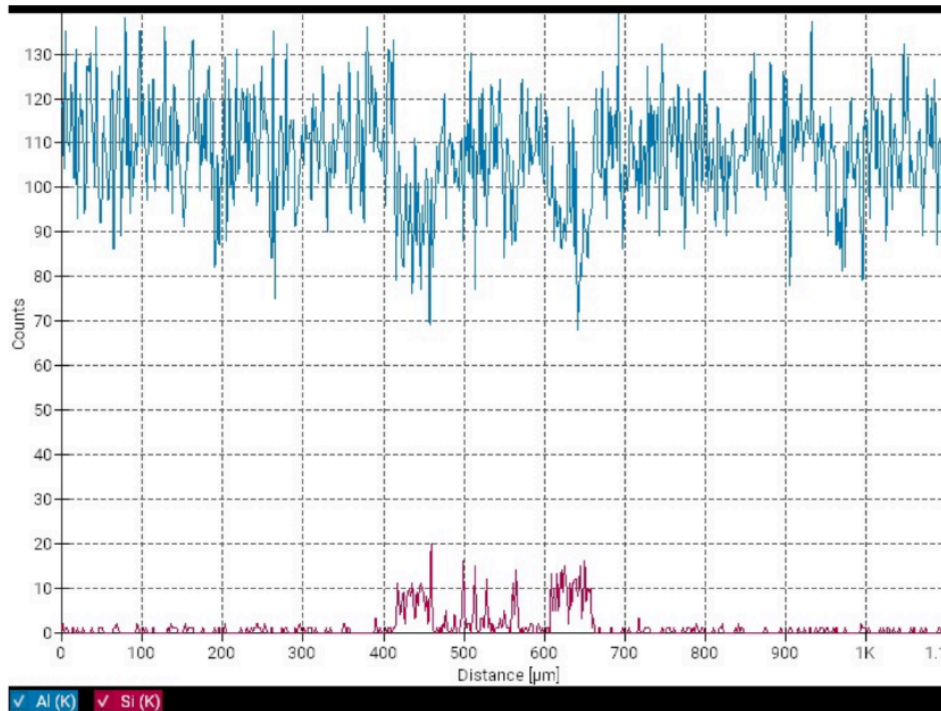
**Figure 36** – SEM images of sample F2 a) 150x; b) 500x ; c) void; d) incomplete filling



Source: the author, 2024.

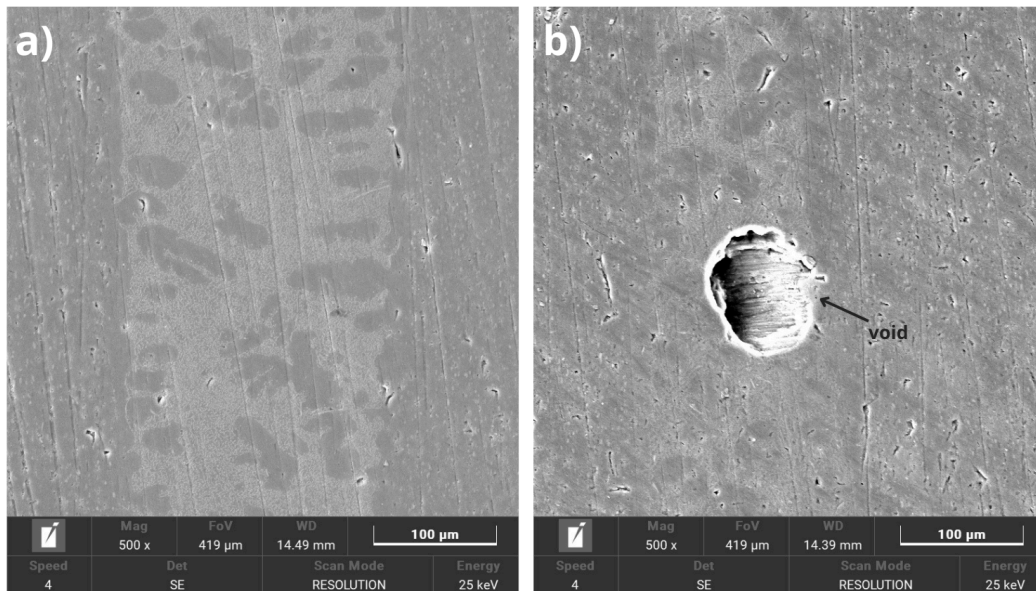
Quantitative EDS analysis of sample F2, in Figure 37, also shows the presence of aluminum and silicon. Induction brazing samples (A2 and F2) showed a more uniform distribution of dendritic arms and eutectic silicon, while flame brazing (C1), Figure 38, showed spherical voids likely due to gas entrapment. These observations suggest that the brazing method may have influence on defects formation and microstructure variations. Induction brazing has a more controlled heating process and seems to result in fewer voids caused by gas when compared to flame brazing, where less controlled conditions may contribute to void formation.

**Figure 37** – EDS of sample F2



Source: the author, 2024.

**Figure 38** – SEM images of sample C1 a) overall; b) void

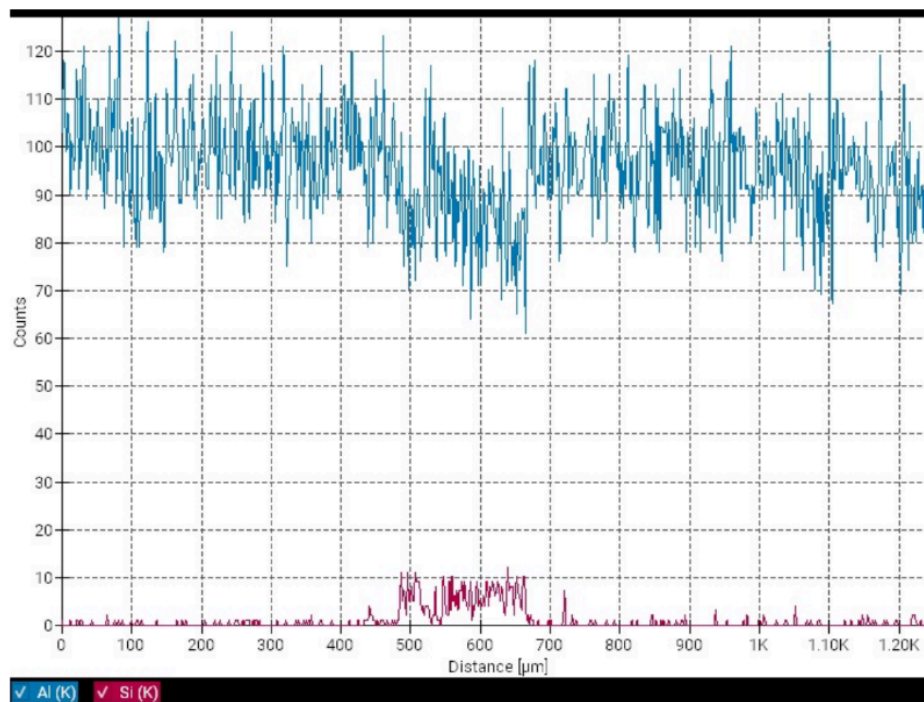


Source: the author, 2024.

According to the semiquantitative analysis of sample C1 (Figure 39), aluminum and silicon were present. The EDS results confirm a consistent concentration of silicon in the

samples, suggesting that silicon plays a crucial role in the microstructure of the joint. Additionally, it enhances fluidity and reduces solidification shrinkage, as noted by Shivaprasad *et al.* (2015)

**Figure 39** – EDS of sample C1



Source: the author, 2024.

#### 4.4 TENSILE TEST

From the tensile test results presented in Table 9, it was observed that all groups showed significant variations in tensile strength and deformation, except for Group IV, which had smaller variation, probably due to the small number of samples in this group. The lowest average tensile strength was 23.70 MPa for Group I, while the highest was 44.78 MPa, corresponding to Group V, which consisted of tubes without brazing or any exposure to temperature, explaining the higher strength observed in this group. Group V also had the highest total strain (0,410 mm/mm), indicating greater ductility, while Group II showed the lowest total strain (0,049 mm/mm).

When comparing Groups I, II, and III, all showed similar tensile strength values, which is consistent with the similar brazing parameters applied to these samples. However,

Group III showed a slight increase in tensile strength compared to Groups I and II, which may be attributed to microstructural factors that influenced the mechanical behavior of the samples. Regarding total strain, Groups II and III had similar results, while Group I showed slightly higher variation. This suggests that, despite the similar brazing parameters for Groups I, II, and III, Group I exhibited greater variability in mechanical properties, possibly due to heterogeneity in brazing quality or differences in individual sample conditions.

The values obtained were lower than the typical values for 3XXX series aluminum alloys, that are usually between 110 to 285 MPa (Kaufman, 2000). However, they are similar to those reported by Kahl *et al.* (2013), who simulated brazing by heating AA3003 alloys, used in heat exchanger tubes, to 600°C for 20 minutes in a controlled atmosphere, followed by a 5-minute hold and then cooling. A tensile strength of  $15.74 \pm 0.09$  MPa was found at room temperature, supporting the observation that the processes might reduce tensile strength due to microstructural changes caused by prolonged heat exposure.

**Table 9** – Average mechanical properties

Sample Group	Ultimate tensile strength - $\sigma_{UTS}$ (MPa)	Standard deviation	Total strain - $\epsilon$ (mm/mm)	Standard deviation
I	23,70	8,69	0,111	0,072
II	23,93	6,83	0,049	0,010
III	28,71	7,87	0,068	0,027
IV	37,17	0,635	0,215	0,040
V	44,78	10,82	0,410	0,085

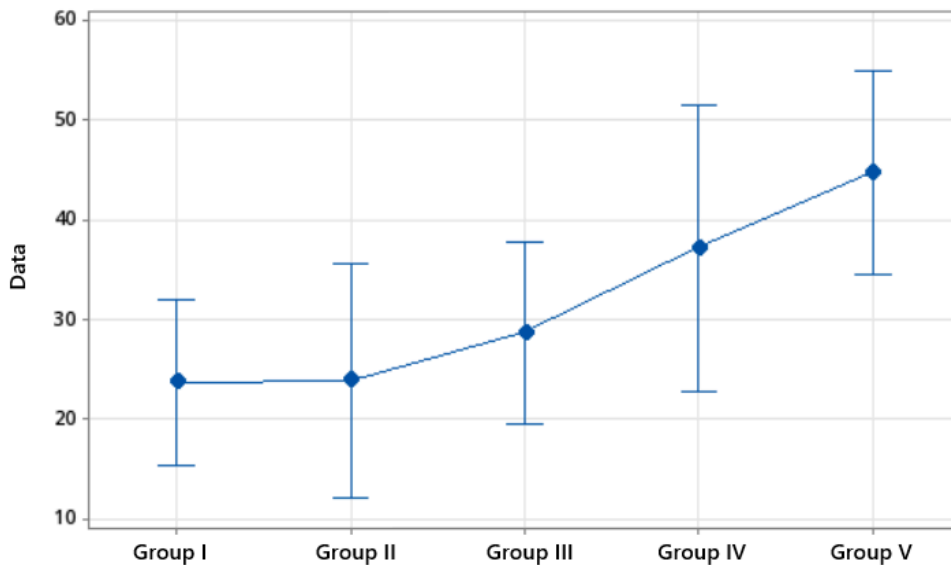
Source: the author, 2024.

The ANOVA test revealed an F-value of 3.62 and a p-value of 0.029 for the tensile strength, indicating significant differences among the group means at a 95% confidence level. Thus, it can be concluded that the variations in the brazing parameters analyzed influenced the mechanical properties of the tubes, with the differences between the group means being statistically significant.

Figure 40 presents the average tensile strength values for Groups I to V, with 95% confidence intervals (CIs) represented by the vertical bars. It shows an increasing trend in tensile strength from Group I to Group V. Group I has the lowest average tensile strength. Groups II and III have similar values, suggesting consistent brazing parameters. Group IV shows a higher average tensile strength and group V, with no brazing, has the highest average

strength. The non-overlapping CIs between some groups indicate statistically significant differences. This suggests that brazing parameters affect the mechanical properties, reducing tensile strength compared to the unbrazed Group V. The graph highlights the impact of brazing on the variability and strength of the samples.

**Figure 40** - Graph of 95% confidence intervals for average tensile strength



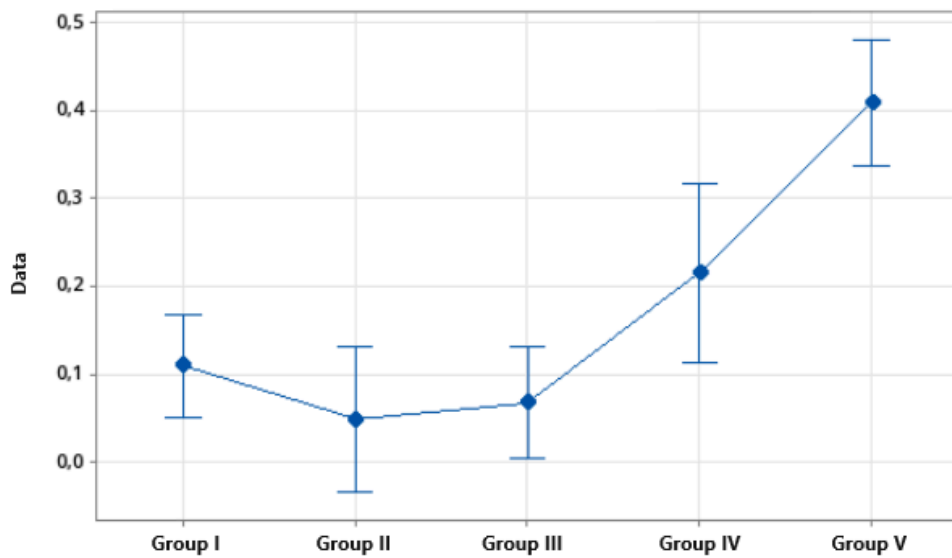
Source: the author, 2024.

For ductility, the ANOVA test revealed an F-value of 19.20 and a p-value of 0.000, indicating statistically significant differences among the group means at a 95% confidence level. These findings confirm that the variations in brazing parameters significantly influenced the deformation properties of the samples. The mean deformation values for Groups I to V, along with their respective 95% confidence intervals (CIs), are presented in Figure 41.

Group II exhibited the lowest mean deformation. Group I displayed a higher mean deformation compared to Group II, with non-overlapping confidence intervals (CIs), indicating a significant difference between these groups. Group III showed a slightly higher deformation than Group II, but with overlapping CIs, suggesting no statistically significant difference between them. Group IV and Group V demonstrated progressively higher deformation values, with no overlap in CIs, highlighting significant differences from the other groups.

The non-overlapping CIs between Groups II, IV, and V allow for a direct comparison, confirming statistically significant differences between these groups. The graph illustrates an increasing trend in deformation from Group II to Group V, suggesting that the absence of brazing (Group V) and specific brazing conditions (Group IV) significantly affect deformation. These results emphasize the role of brazing parameters in modulating deformation behavior and variability across the samples.

**Figure 41** - Graph of 95% confidence intervals for average deformation

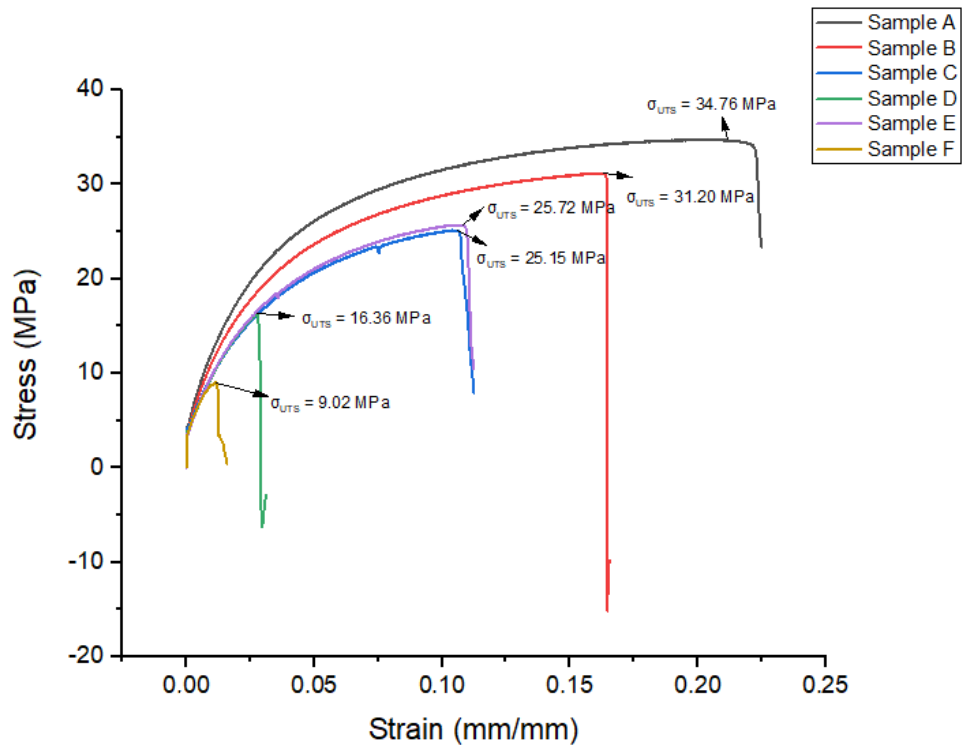


Source: the author, 2024.

Figures 42 to 47 show the stress-strain curves for each sample within their respective groups. In Group I (Figure 42), the variation in strength and strain values between the samples is evident. Samples A, B, C, D, and E did not fracture at the joint but failed in the heat-affected zone of the tube, as shown in Figure 43a, indicating that the joint can withstand more force than the tube itself. This result suggests that, at the point of rupture, the stress in the brazed region was lower than in the tube material, with the joint being strong enough to transfer the stress to the tube, resulting in failure outside the joint.

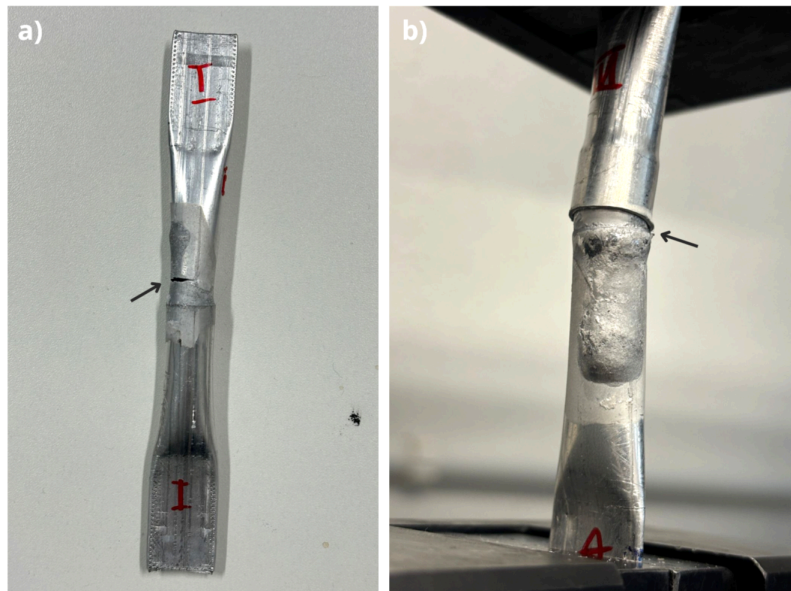


**Figure 42 – Stress Strain Curves for Group I**



Source: the author, 2024.

**Figure 43 – Observed failure in Group I a) sample A; b) sample F**

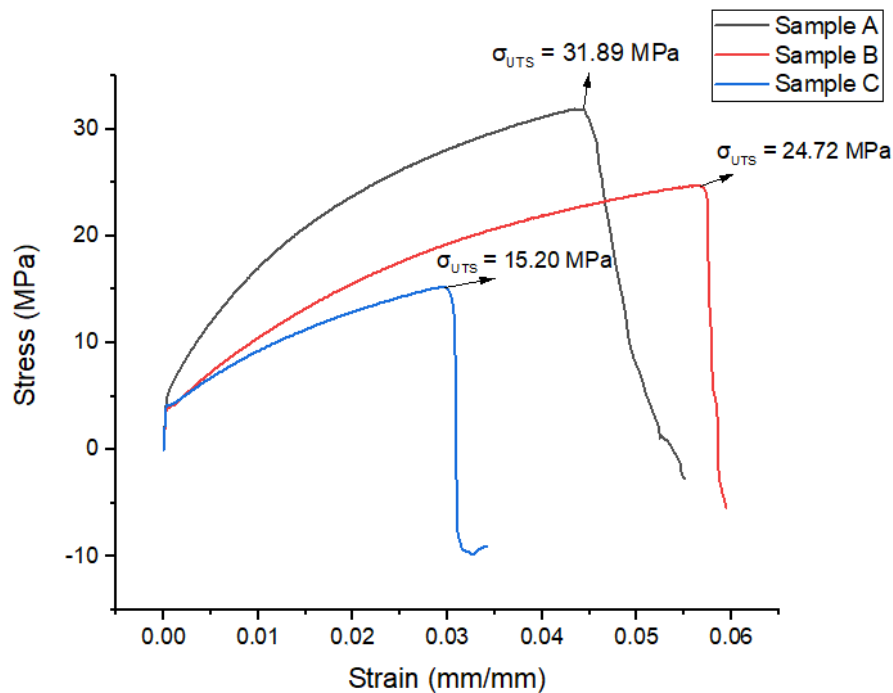


Source: the author, 2024.

This conclusion is supported by the fact that the tension was calculated using the tube's cross-sectional area, which is smaller than from the brazed region. However, Sample F failed at the joint, as shown in Figure 43b, resulting in the detachment of the two tube sections. In this case, it may be worthwhile to calculate the tension specifically in the brazed region to better understand the joint's strength relative to the tube. In this case the area of the brazed joint is around 55,49 mm<sup>2</sup> and the tension is 4,32 MPa and it is the lower tension between the samples from Group I.

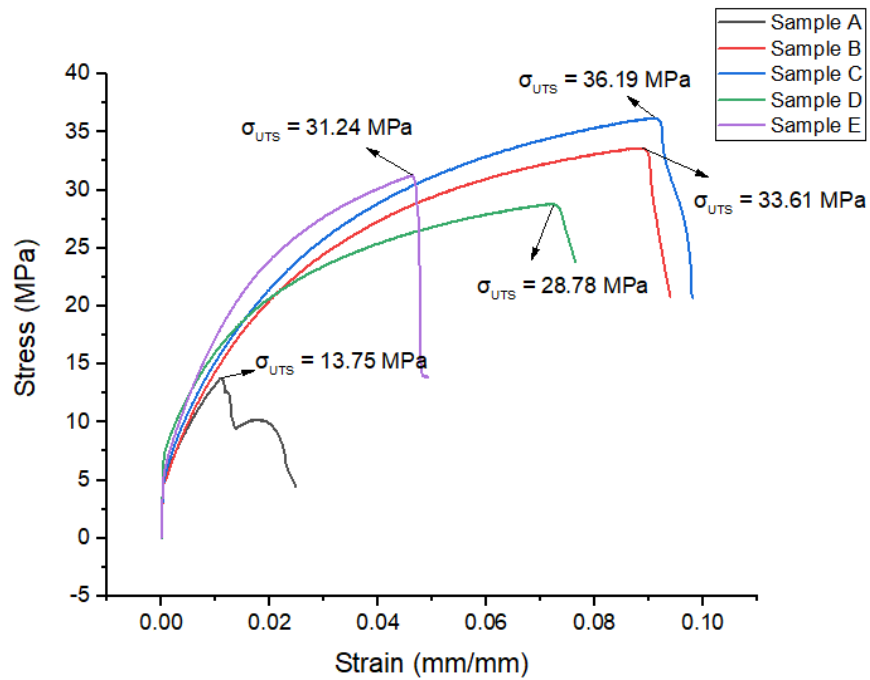
In Groups II and III (Figures 44 and 45, respectively), all samples fractured in the heat-affected zone of the tube. The notably low tensile strength of Sample C from Group II (15.20 MPa) and Sample A from Group III (13.75 MPa) could be attributed to potential irregularities in the manufacturing process, such as variations in temperature control during brazing, or internal defects like porosity or solute segregation.

**Figure 44** – Stress Strain Curves for Group II



Source: the author, 2024.

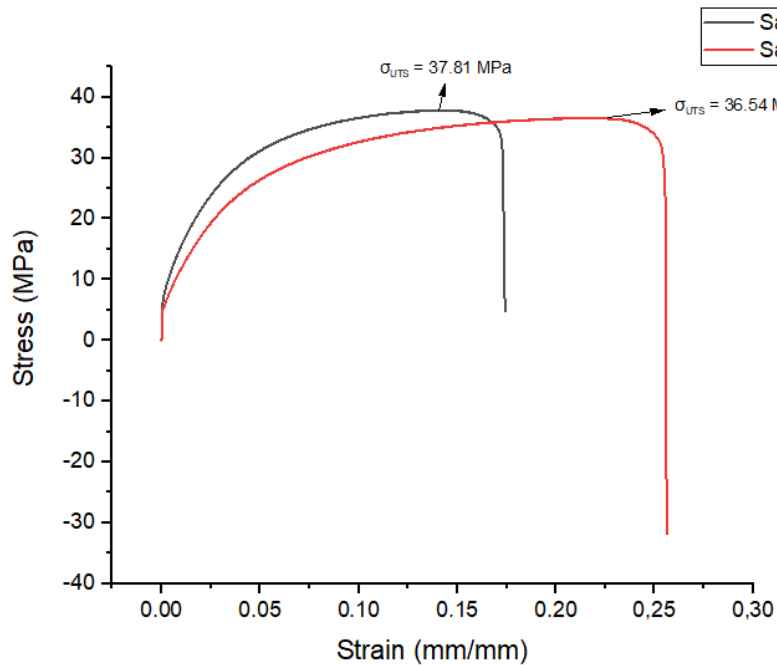
**Figure 45 – Stress Strain Curves for Group III**



Source: the author, 2024.

In Group IV (Figure 46), the tubes fractured outside the heat-affected zone, leading to slightly higher tensile strength values compared to Groups I, II, and III.

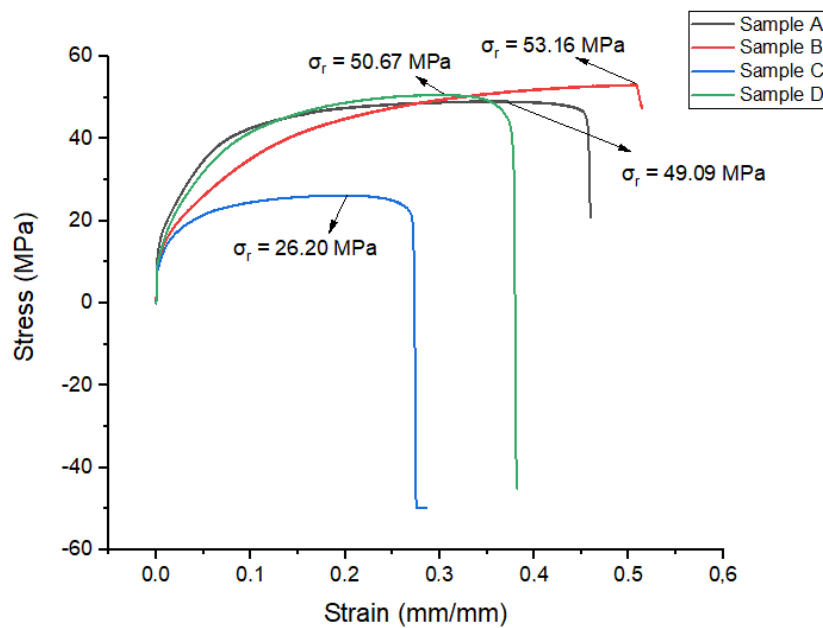
**Figure 46 – Stress Strain Curves for Group IV**



Source: the author, 2024.

Group V (Figure 47) represents the unbrazed tubes, which exhibited higher tensile strength than any other group. This suggests that the exposure to heat had a direct impact on mechanical behavior, reducing both tensile strength and ductility in the tubes. The influence of temperature on the brazed groups is evident, as both tensile strength and total strain of the brazed tubes were significantly lower compared to the group of unbrazed tubes.

**Figure 47 – Stress Strain Curves for Group V**



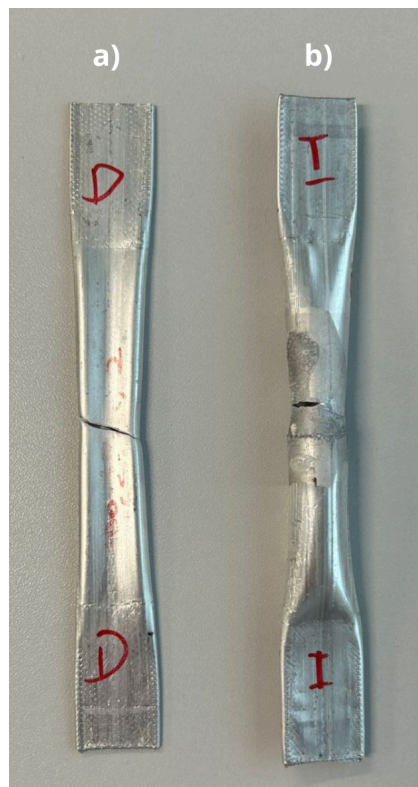
Source: the author, 2024.

After analyzing the stress-strain curves and discussing the mechanical behavior of the samples, attention turns to the characteristics of the fractures observed. In the case of the tube without brazing, represented by fracture in Figure 48a, the failure occurs at an angle of approximately 45 degrees. This fracture angle is characteristic of ductile materials subjected to shear stress during tensile loading. It indicates uniform deformation leading to ductile rupture, with the material suffering significant plastic deformation before breaking. The absence of a brazed joint ensures that the mechanical strength is entirely dependent on the aluminum alloy 3103 base material, which has any alterations caused by heat.

In contrast, the fracture in the brazed joint, represented by fracture in Figure 48b, occurs at a 90-degree angle to the loading direction. This perpendicular fracture suggests a more brittle failure mechanism, normally associated with localized weaknesses in the

material. The brazing process creates a heat-affected zone (HAZ) around the joint, where microstructural changes such as solute segregation, porosity, or the formation of brittle phases may occur. These alterations reduce the mechanical strength of the brazed region, making it the preferential site for failure. Unlike the base material, the brazed joint does not exhibit significant plastic deformation before fracture, reflecting the lower mechanical performance of the joint compared to the base tube material.

**Figure 48** – Fracture surfaces of aluminum tubes a) without and b) with brazing



Source: the author, 2024.

The information of tensile strength is important as it can be used to estimate the pressure these tubes would withstand. According to Lamé's equation, the pressure is calculate in terms of tube's diameter ( $D$ ), thickness ( $t$ ) and tensile strength ( $\sigma_{UTS}$ ) (Cheng, Wu and Ma, 2015).

$$P = \frac{2 \cdot \sigma_{UTS} \cdot t}{D} \quad (6)$$

Equation (7) incorporates a factor  $4/\sqrt{3}$  of which aligns with the von Mises yield criterion. This approach provides a more conservative estimate of the maximum allowable pressure, accounting for the triaxial stress state that typically occurs in ductile materials under internal pressure.

$$P = \frac{4 \cdot \sigma_{UTS} \cdot t}{\sqrt{3}D} \quad (7)$$

**Table 10** – Maximum Allowable Pressure Based on Tensile Strength

Group	$\sigma_{UTS}$ (MPa)	P (MPa)	P (bar)
I	23.70	2.68	26.8
II	23.93	2.70	27
III	28.71	4.06	40.6
IV	37.17	4.20	42
V	44.78	5.06	50.6

Source: the author, 2024.

From Table 10, considering the fluids that may flow through these tubes, with application pressures ranging from 4 to 28 bar, most of the joints would withstand the expected conditions, except for joints I and II under the maximum pressure. However, for applications involving fluids at lower pressures, such as those below 26 bar, joints I and II would still perform adequately and meet safety requirements.

## 5 CONCLUSION

This study investigated the induction brazing process of aluminum tubes from the alloy 3103 with filler metal 4047A, seeking application in heat exchangers. The comparative analysis of the techniques of flame and induction allowed identification of specific advantages of induction brazing, such as reduction of time and directed heating, factors that contributed to a smaller amount of defects. From the development of a copper inductor for the induction process, it was possible to obtain efficient and uniform heating, with the 2.NY 287 being the best option. This thermal control was improved by the two-step methodology, where the process starts with higher power and then goes lower to avoid overheating, standing out as the most effective approach to speed up the process.

Microstructural analyses performed by optical microscopy and SEM showed that, in most samples, there was a good distribution of the filler material. Although some samples presented good distribution, others contained areas with incomplete filling, which can negatively impact the durability of the heat exchanger due to the risk of corrosion, as observed in samples B1, F1, F2, G1 and G2, which received a lower amount of heat. The samples that showed the best filling/brazing time ratio were A1 and A2, thus, the induction parameters of 100% for 10 s, followed by 65% for the remaining time, with a 6  $\mu$ F capacitor, 15.8 kHz frequency and 8  $\mu$ s minimum gap were considered the most appropriate. While for tube B, the best condition was 100% for 10 s, followed by 67% for the remaining time, with the same capacitor, frequency and minimum gap of tube A.

Furthermore, dendritic structures typical of hypoeutectic alloys were observed, as well as the interface between the alloys. EDS showed the distribution and composition of the elements along the joint, confirming the presence of aluminum and silicon in the fusion area.

The tensile tests revealed that the strength of the brazed joints is sufficient to withstand significant loads, reaching 37.81 MPa, a value consistent with other references, although lower than the strength of the unbrazed tube, which reached 53.16 MPa. The stress-strain curves showed that the brazed samples withstood significant forces without fracturing at the joint, with the fracture occurring outside the joint region, suggesting that the strength of the joint was greater than that of the tube itself. As for the strain the lowest value achieved was 0.049 mm/mm for group II, and highest deformation was 0.410 mm/mm, from group V. The maximum pressure that the tube can withstand was calculated using the Lamé equation, resulting in values suitable for applications requiring pressures of up to 28 bar. Although joints I and II have lower allowable pressures, they remain adequate for applications involving lower operating pressures, with the lowest calculated allowable pressure being 26.8 bar.

In summary, the induction brazing method, especially with the two-step methodology, offers a promising path for the fabrication of aluminum heat exchanger joints, providing better process control and reducing the risk of structural defects. However, specific adjustments to the brazing parameters are still required to ensure the consistency and durability of brazed joints in demanding operating environments.

## 6 RECOMMENDATIONS FOR FUTURE WORK

- Measure the primary, secondary, and tertiary dendritic spacing: This spacing can influence key properties of the samples, such as hardness, ductility, and corrosion resistance, providing a more detailed understanding of the brazed joint microstructure;
- Prepare a greater number of flame-brazed samples: Increase the sample quantity to achieve a more robust comparison, including the performance of tensile tests;
- Conduct leak tests: Evaluate the sealing of brazed joints to ensure reliability in applications where integrity is essential for the heat exchanger's functionality;
- Study the corrosion resistance of brazed joints in environments that simulate heat exchanger conditions, focusing on the durability and resistance of materials to various fluids and corrosive media;
- Explore the use of alternative filler metals in brazing to evaluate their impact on joint properties, including mechanical strength, thermal performance, and corrosion resistance, offering potential for optimization in specific applications.



## REFERÊNCIAS

- AMERICAN NATIONAL STANDARDS INSTITUTE. **H35.1/H35.1M**: American National Standard Alloy and Temper Designation Systems for Aluminum. Arlington: The Aluminum Association, Inc., 2017.
- CALÇADA, Maurício Vieira. **AVALIAÇÃO MECÂNICA E MICROESTRUTURAL DA LIGA DE ALUMÍNIO AA3104 EMPREGADA NA INDÚSTRIA DE FABRICAÇÃO DE LATAS LAMINADA À FRIO COM E SEM INTERPASSES**. 2018. 85 f. Dissertação (Mestrado) - Curso de Engenharia Mecânica, Universidade Estadual Paulista, Guaratinguetá, 2018.
- ÇAM, Gürel; İPEKOĞLU, Güven. Recent developments in joining of aluminum alloys. **The International Journal Of Advanced Manufacturing Technology**, [S.L.], v. 91, n. 5-8, p. 1851-1866, 24 dez. 2016. Springer Science and Business Media LLC. <http://dx.doi.org/10.1007/s00170-016-9861-0>.
- CHEN, Rui; SHI, Yu-Feng; XU, Qing-Yan; LIU, Bai-Cheng. Effect of cooling rate on solidification parameters and microstructure of Al-7Si-0.3Mg-0.15Fe alloy. **Transactions Of Nonferrous Metals Society Of China**, [S.L.], v. 24, n. 6, p. 1645-1652, jun. 2014. Elsevier BV. [http://dx.doi.org/10.1016/s1003-6326\(14\)63236-2](http://dx.doi.org/10.1016/s1003-6326(14)63236-2).
- CHENG, Wei-Yang; WU, Shinn-Dar; MA, Hsiao-Kang. Study of tensile strength of aluminum alloy bottle with carbon fiber winding. **International Journal Of Hydrogen Energy**, [S.L.], v. 40, n. 36, p. 12436-12446, set. 2015. Elsevier BV. <http://dx.doi.org/10.1016/j.ijhydene.2015.07.052>.
- DIAS FILHO, José Marcelino; KIKUCHI, Rafael Hideo; COSTA, Thiago Antônio Paixão de Sousa; MOREIRA, Antonio Luciano Seabra; ROCHA, Otávio Fernandes Lima da. Influência das Variáveis Térmicas Sobre os Espaçamentos Dendríticos Terciários durante a Solidificação Direcional Horizontal da Liga Al-6%Cu. **Matéria (Rio de Janeiro)**, [S.L.], v. 20, n. 1, p. 47-63, mar. 2015. FapUNIFESP (SciELO). <http://dx.doi.org/10.1590/s1517-707620150001.0008>.
- DU, Q.; POOLE, W.J.; WELLS, M.A.; PARSON, N.C.. Microstructure evolution during homogenization of Al-Mn-Fe-Si alloys: modeling and experimental results. **Acta Materialia**, [S.L.], v. 61, n. 13, p. 4961-4973, ago. 2013. Elsevier BV. <http://dx.doi.org/10.1016/j.actamat.2013.04.050>.
- DYBOWSKI, Bartłomiej; POLOCZEK, Łukasz; KIEBUS, Andrzej. The Porosity Description in Hypoeutectic Al-Si Alloys. **Key Engineering Materials**, [S.L.], v. 682, p. 83-90, 15 fev. 2016. Trans Tech Publications, Ltd.. <http://dx.doi.org/10.4028/www.scientific.net/kem.682.83>.
- ENGLER, Olaf; BRÜGGEMANN, Thiemo; HASENCLEVER, Jochen. Evolution of micro-chemistry during solidification and homogenisation of AA 3xxx aluminium-manganese alloys. **Materials Science And Technology**, [S.L.], v. 37, n. 10, p. 893-908, jul. 2021. SAGE Publications. <http://dx.doi.org/10.1080/02670836.2021.1963540>.

FERRARINI, Cleyton Fernandes. **Microestrutura e Propriedades Mecânicas de Ligas Al-Si Hipoeutéticas Conformadas por Spray**. 2005. 108 f. Tese (Doutorado) - Curso de Engenharia de Materiais, São Carlos, São Carlos, 2005.

GOMES, Leonardo Fernandes; KUGELMEIER, Cristie Luis; GARCIA, Amauri; DELLA ROVERE, Carlos Alberto; SPINELLI, José Eduardo. Influences of alloying elements and dendritic spacing on the corrosion behavior of Al–Si–Ag alloys. **Journal Of Materials Research And Technology**, [S.L.], v. 15, p. 5880-5893, nov. 2021. Elsevier BV. <http://dx.doi.org/10.1016/j.jmrt.2021.11.043>.

HAUS, J. P.. Induction brazing – old process with potential innovations. **Welding International**, [S.L.], v. 22, n. 5, p. 329-334, maio 2008. Informa UK Limited. <http://dx.doi.org/10.1080/09507110802200705>.

HOSCH, T.; NAPOLITANO, R.e.. The effect of the flake to fiber transition in silicon morphology on the tensile properties of Al–Si eutectic alloys. **Materials Science And Engineering: A**, [S.L.], v. 528, n. 1, p. 226-232, nov. 2010. Elsevier BV. <http://dx.doi.org/10.1016/j.msea.2010.09.008>.

Inspection/Test Certificate. Hydro. Order number: 4500028519, 2021.

INTERNATIONAL ORGANIZATION FOR STANDARDIZATION. **18279**: Brazing — Imperfections in brazed joints. 2 ed. [S.I]: Iso, 2023.

INTERNATIONAL ORGANIZATION FOR STANDARDIZATION. **9454-1**: Soft soldering fluxes — Classification and requirements Part 1: Classification, labelling and packaging. 2 ed. [S.I]: Iso, 2016.

JACOBSON, David M.; HUMPSTON, Giles. **Principles of Brazing**. Ohio: Asm International, 2005.

KAHL, Sören; EKSTRÖM, Hans-Erik; MENDOZA, Jesus. Tensile, Fatigue, and Creep Properties of Aluminum Heat Exchanger Tube Alloys for Temperatures from 293 K to 573 K (20 °C to 300 °C). **Metallurgical And Materials Transactions A**, [S.L.], v. 45, n. 2, p. 663-681, 25 set. 2013. Springer Science and Business Media LLC. <http://dx.doi.org/10.1007/s11661-013-2003-5>.

KAKITANI, Rafael. **Evolução Microestrutural, Dureza e Resistência à Corrosão de Ligas Ternárias do Sistema Al-Si-Zn Utilizadas em Brasagem**. 2021. 123 f. Tese (Doutorado) - Curso de Engenharia Mecânica, Universidade Estadual de Campinas, Campinas, 2021.

KAUFMAN, John Gilbert. **Introduction to Aluminum Alloys and Tempers**. [S.I]: Asm International, 2000.

KADHIM, Zeyad D.. EFFECT OF COOLING RATE ON MECHANICAL PROPERTIES OF EUTECTIC AND HYPOEUTECTIC Al-Si ALLOYS. **Journal Of Engineering**, [S.L.], v. 17, n. 06, p. 1576-1583, 1 dez. 2011. Journal of Engineering.

LANZUTTI, Alex; ANDREATTA, Francesco; MAGNAN, Michele; FEDRIZZI, Lorenzo. Microstructural and in-depth electrochemical characterization of Zn diffusion layers on

aluminum 3xxx alloy. **Surface And Interface Analysis**, [S.L.], v. 51, n. 12, p. 1165-1172, 16 dez. 2018. Wiley. <http://dx.doi.org/10.1002/sia.6602>.

LI, Feng; LI, Xue Kun; ZHU, Tian Xing; ZHAO, Qian Zhe; RONG, Yi Ming Kevin. Modeling and Simulation of Induction Heating with Magnetic Flux Concentrator. **Applied Mechanics And Materials**, [S.L.], v. 268-270, p. 983-991, dez. 2012. Trans Tech Publications, Ltd.. <http://dx.doi.org/10.4028/www.scientific.net/amm.268-270.983>.

LI, Yuxiang; CHEN, Chao; YI, Ruixiang; OUYANG, Yawen. Review: special brazing and soldering. **Journal Of Manufacturing Processes**, [S.L.], v. 60, p. 608-635, dez. 2020. Elsevier BV. <http://dx.doi.org/10.1016/j.jmapro.2020.10.049>.

LIANG, Min; QIN, Youqiong; ZHANG, Danfeng; ZHAO, Feng. Effect of Brazing Clearance on the Microstructure and Mechanical Properties of TC4/TC4 Joints Brazed in Vacuum with Ti-Zr-Ni Filler Metal. **Journal Of Materials Engineering And Performance**, [S.L.], v. 32, n. 7, p. 2973-2982, 9 set. 2022. Springer Science and Business Media LLC. <http://dx.doi.org/10.1007/s11665-022-07295-1>.

MILANI, Seyyed Ali Akbar Hashemi; TAVANGAR, Reza; AZADBEH, Mazyar. Effect of NOCOLOK® flux dry-off temperature on mechanical properties of brazed joint for automotive aluminum-based heat exchangers. **Engineering Research Express**, [S.L.], v. 2, n. 2, p. 025003, 6 abr. 2020. IOP Publishing. <http://dx.doi.org/10.1088/2631-8695/ab82eb>.

MOEMA, Joseph S.; SIYASIYA, Charles W.; MORUDU, Veronica K.; BUTHELEZI, Thokozani. The Effect of Soaking Time on Mechanical Properties of Roll-Bonded AA3003 and AA4045 Used for Heat Exchangers. **Metals**, [S.L.], v. 13, n. 10, p. 1636, 23 set. 2023. MDPI AG. <http://dx.doi.org/10.3390/met13101636>.

MOSCHINGER, Matthias; VAUDERWANGE, Thomas; ENZINGER, Norbert. Plasma wire arc additive manufacturing and its influence on high-carbon steel substrate properties. **Welding In The World**, [S.L.], v. 68, n. 8, p. 1999-2011, 12 fev. 2024. Springer Science and Business Media LLC. <http://dx.doi.org/10.1007/s40194-024-01717-5>.

PETER, Hans-Joachim. **Handbuch Induktives Löten**. Berlin: Peter, 2014.

RAJI, Nurudeen Adekunle; OLUWOLE, Oluleke Olugbemiga. Effect of Soaking Time on the Mechanical Properties of Annealed Cold-Drawn Low Carbon Steel. **Materials Sciences And Applications**, [S.L.], v. 03, n. 08, p. 513-518, 2012. Scientific Research Publishing, Inc.. <http://dx.doi.org/10.4236/msa.2012.38072>.

RÓŜAŃSKI, Maciej; RĘKASOWSKI, Piotr. Application of induction heating in brazing processes. **Welding International**, [S.L.], v. 26, n. 4, p. 282-285, abr. 2012. Informa UK Limited. <http://dx.doi.org/10.1080/09507116.2011.600001>.

RUDNEV, Valery; LOVELESS, Don; COOK, Raymond L.. **Handbook of Induction Heating**. Crc Press, 2017.

SHEN, W.; HU, A.; LIU, S.; HU, H.. Al-Mn alloys for electrical applications: a review. **Journal Of Alloys And Metallurgical Systems**, [S.L.], v. 2, p. 100008, jun. 2023. Elsevier BV. <http://dx.doi.org/10.1016/j.jalmes.2023.100008>.

SHIVAPRASAD, C.G.; AITHAL, Kiran; NARENDRANATH, S.; DESAI, Vijay; MUKUNDA, P.G.. Effect of combined grain refinement and modification on microstructure and mechanical properties of hypoeutectic, eutectic and hypereutectic Al-Si alloys. **International Journal Of Microstructure And Materials Properties**, [S.L.], v. 10, n. 3/4, p. 274, 2015. Inderscience Publishers. <http://dx.doi.org/10.1504/ijmmp.2015.072921>.

SCHWARTZ, Mel M.. **Brazing**. 2. ed. Uni: Asm International, 2003.

SIGWORTH, Geoffrey K.. Fundamentals of Solidification in Aluminum Castings. **International Journal Of Metalcasting**, [S.L.], v. 8, n. 1, p. 7-20, jan. 2014. Springer Science and Business Media LLC. <http://dx.doi.org/10.1007/bf03355567>.

SILVA JUNIOR, Moisés Euclides da. **FABRICAÇÃO DAS LIGAS DE ALUMÍNIO AA3003 E AA3303 A PARTIR DOS PÓS ELEMENTARES DE ALUMÍNIO E DE MANGANÊS ATRAVÉS DE TÉCNICAS DE METALURGIA DO PÓ**. 2020. 127 f. Tese (Doutorado) - Curso de Engenharia Mecânica, Universidade Federal de Pernambuco, Recife, 2020.

SINGH, Akhilesh Kumar; DEY, Vidyut; RAI, Ram Naresh. Techniques to improve weld penetration in TIG welding (A review). **Materials Today: Proceedings**, [S.L.], v. 4, n. 2, p. 1252-1259, 2017. Elsevier BV. <http://dx.doi.org/10.1016/j.matpr.2017.01.145>.

SIQUEIRA, Lucas Oliveira. **BRASAGEM DE AÇO INOXIDÁVEL AUSTENÍTICO COM METAIS DE ADIÇÃO À BASE DE PRATA PARA APLICAÇÃO EM SISTEMAS PRESSURIZADOS DE AERONAVES**. 2021. 106 f. Dissertação (Mestrado) - Curso de Engenharia e Ciências Aeroespaciais, Universidade Federal de Pernambuco, Recife, 2021.

SOBRAL, Bruno Silva. **Solidificação Direcional, Microestrutura e Microdureza da liga eutética Sn-3,5%Ag modificada por Zn**. 2021. 89 f. Tese (Doutorado) - Curso de Ciência e Engenharia de Materiais, Universidade Federal do Rio Grande do Norte, Natal, 2021.

Technical Data Sheet. LucasMilhaupt. FILALU 1192 NC / NCF / NCM, 2023.

VOZNIAKI, Márcio Luis. **ESTUDO COMPARATIVO DA BRASAGEM DE ALUMÍNIO COM DIFERENTES MEIOS DE ADIÇÃO**. 2014. 52 f. TCC (Graduação) - Curso de Engenheiro Mecânico, Universidade Tecnológica Federal do Paraná, Ponta Grossa, 2014.

WAY, Matthew; WILLINGHAM, Jack; GOODALL, Russell. Brazing filler metals. **International Materials Reviews**, [S.L.], v. 65, n. 5, p. 257-285, 14 maio 2019. SAGE Publications. <http://dx.doi.org/10.1080/09506608.2019.1613311>.

WEN, Huaiyu; ZHANG, Xiaobo; YE, Hugen; HAN, Yi. Research on the mechanism of magnetic flux concentrator in the gap-to-gap induction heating of wind power gear. **International Journal Of Thermal Sciences**, [S.L.], v. 168, p. 107055, out. 2021. Elsevier BV. <http://dx.doi.org/10.1016/j.ijthermalsci.2021.107055>.

ZAZYCKI, Eduardo Augusto; SOUZA, Vinicius Pereira; LAMPERT, Vinicius Renan; DALCIN, Rafael Luciano. União de tubos hidráulicos de alta pressão por brasagem: estudo

de caso. In: **SEMANA INTERNACIONAL DAS ENGENHARIAS E ECONOMIA FAHOR**, 7., 2017, Horizontina, RS.

ZHAO, Pengcheng; ZHAO, Liangyin; TAN, Long; XU, Zhisen; WANG, Lulu; ZHAO, Xiuxiu. Investigation on the induction brazing of copper–steel tubes with different coil structures. **Welding In The World**, [S.L.], v. 65, n. 6, p. 1181-1188, 26 jan. 2021. Springer Science and Business Media LLC. <http://dx.doi.org/10.1007/s40194-021-01074-7>.

ZHAO, Hui; ELBEL, Stefan; HRNJAK, Pega. Low Melting Temperature Brazing Materials for Aluminum Heat Exchanger Fabrication. In: THE INTERNATIONAL REFRIGERATION AND AIR CONDITIONING CONFERENCE, 18., 2021, West Lafayette. **Proceedings [...]** . West Lafayette: Purdue E-Pubs, 2021. p. 1-8.